

**AWARD NUMBER: W81XWH-15-1-0341**

**TITLE:** High Spatiotemporal Resolution Prostate MRI

**PRINCIPAL INVESTIGATOR:** Stephen J. Riederer

**CONTRACTING ORGANIZATION:** Mayo Clinic  
Rochester, MN 55905-0002

**REPORT DATE:** NOVEMBER 2018

**TYPE OF REPORT:** Final

**PREPARED FOR:** U.S. Army Medical Research and Materiel Command  
Fort Detrick, Maryland 21702-5012

**DISTRIBUTION STATEMENT:** Approved for Public Release; Distribution Unlimited

The views, opinions and/or findings contained in this report are those of the author(s) and should not be construed as an official Department of the Army position, policy or decision unless so designated by other documentation.

<b>REPORT DOCUMENTATION PAGE</b>			<i>Form Approved</i> <i>OMB No. 0704-0188</i>		
Public reporting burden for this collection of information is estimated to average 1 hour per response, including the time for reviewing instructions, searching existing data sources, gathering and maintaining the data needed, and completing and reviewing this collection of information. Send comments regarding this burden estimate or any other aspect of this collection of information, including suggestions for reducing this burden to Department of Defense, Washington Headquarters Services, Directorate for Information Operations and Reports (0704-0188), 1215 Jefferson Davis Highway, Suite 1204, Arlington, VA 22202-4302. Respondents should be aware that notwithstanding any other provision of law, no person shall be subject to any penalty for failing to comply with a collection of information if it does not display a currently valid OMB control number. <b>PLEASE DO NOT RETURN YOUR FORM TO THE ABOVE ADDRESS.</b>					
<b>1. REPORT DATE</b> NOVEMBER 2018		<b>2. REPORT TYPE</b> Final		<b>3. DATES COVERED</b> 15 August 2015 – 14 August 2018	
<b>4. TITLE AND SUBTITLE</b>  High Spatiotemporal Resolution Prostate MRI			<b>5a. CONTRACT NUMBER</b>		
			<b>5b. GRANT NUMBER</b> W81XWH-15-1-0341		
			<b>5c. PROGRAM ELEMENT NUMBER</b>		
<b>6. AUTHOR(S)</b>  Stephen J. Riederer  E-Mail: Riederer@mayo.edu			<b>5d. PROJECT NUMBER</b>		
			<b>5e. TASK NUMBER</b>		
			<b>5f. WORK UNIT NUMBER</b>		
<b>7. PERFORMING ORGANIZATION NAME(S) AND ADDRESS(ES)</b>  Mayo Clinic 200 1 <sup>st</sup> ST SW Rochester, MN 55905-0002			<b>8. PERFORMING ORGANIZATION REPORT NUMBER</b>		
<b>9. SPONSORING / MONITORING AGENCY NAME(S) AND ADDRESS(ES)</b>  U.S. Army Medical Research and Materiel Command Fort Detrick, Maryland 21702-5012			<b>10. SPONSOR/MONITOR'S ACRONYM(S)</b>		
			<b>11. SPONSOR/MONITOR'S REPORT NUMBER(S)</b>		
<b>12. DISTRIBUTION / AVAILABILITY STATEMENT</b>  Approved for Public Release; Distribution Unlimited					
<b>13. SUPPLEMENTARY NOTES</b>					
<b>14. ABSTRACT</b>  Prostate cancer (PCa) is the second leading cause of cancer death in men. However, when detected and treated promptly the five-year relative survival rate approaches 100%. The overall purpose of this project is to develop improved means using MRI for detecting prostate cancer with the potential for differentiating disease aggressiveness. The hypothesis is that dynamic whole-volume contrast-enhanced perfusion imaging of the prostate gland can be performed with 1 mm isotropic spatial resolution and 2 sec frame times, providing an order of magnitude improvement over current techniques. The specific aims are: (i) to develop an MRI acquisition technique for time-resolved 3D MRI of the prostate, (ii) to develop a fundamentally new coil element family having variable sensitivity along the superior-to-inferior direction, (iii) to incorporate partial Fourier and acceleration methods into high speed reconstruction to provide high quality 3D images in real time at frame times of 2 sec or less.					
<b>15. SUBJECT TERMS</b>  Prostate Cancer, Dynamic-Contrast-Enhanced Prostate MRI					
<b>16. SECURITY CLASSIFICATION OF:</b>			<b>17. LIMITATION OF ABSTRACT</b>	<b>18. NUMBER OF PAGES</b>	<b>19a. NAME OF RESPONSIBLE PERSON</b> USAMRMC
<b>a. REPORT</b>	<b>b. ABSTRACT</b>	<b>c. THIS PAGE</b>			<b>19b. TELEPHONE NUMBER</b> (include area code)
Unclassified	Unclassified	Unclassified	Unclassified	38	

**TABLE OF CONTENTS**

	<u>Page</u>
1. Introduction	4
2. Keywords	4
3. Accomplishments	4
4. Impact	14
5. Changes/Problems	14
6. Products	15
7. Participants & Other Collaborating Organizations	16
8. Special Reporting Requirements	17
9. Appendices (Listing)	17

## 1. INTRODUCTION

Prostate cancer (PCa) is the second leading cause of cancer death in men after lung cancer. Approximately one in nine men will be diagnosed with prostate cancer but when detected early and treated promptly the five-year relative survival rate approaches 100%. The motivation of this project is to develop improved means for detecting prostate cancer. Magnetic resonance imaging (MRI) has been applied to the imaging of prostate cancer for several decades. The typical MRI prostate exam today consists of several “pulse sequences:” (i) T2-weighted spin-echo imaging; (ii) diffusion-weighted imaging (DWI); (iii) dynamic contrast-enhanced (DCE) perfusion MRI. While prostate cancer can be visualized using each sequence, only sequence (iii) provides dynamic information about the temporal enhancement pattern of any PCa lesions. The purpose of this project is to develop 10× improved spatiotemporal resolution DCE-MRI of prostate.

## 2. KEYWORDS

ADC	Apparent Diffusion Coefficient
CAPR	Cartesian Acquisition with Projection Reconstruction-like Sampling
CE-MRA	Contrast-Enhanced Magnetic Resonance Angiography
DCE-MRI	Dynamic-Contrast-Enhanced Magnetic Resonance Imaging
MRI	Magnetic Resonance Imaging
PCa	Prostate Cancer
SENSE	Sensitivity Encoding (a type of MRI acceleration technique)
SNR	Signal-to-Noise Ratio

## 3. ACCOMPLISHMENTS:

### What were the major goals of the project?

Tasks for Months 1-36 (encompassing August 15, 2015 through August 14, 2018) taken from the grant application Statement of Work are shown below. Completed tasks reported in the July 2016 Progress Report are shown with the month of completion in **blue (in parentheses)**. Completed tasks reported in the July 2017 Progress Report with the completion month are shown in **red**. Tasks completed within the time since the July 2017 report are shown in **green**.

Specific Aim 1: Development of MRI Acquisition Method	Months	Investigator
Major Task 1: Optimization of pCAPR Pulse Sequence Applied to Prostate Imaging		
Subtask 1.1: Determine parameter options for various spatiotemporal resolution combinations	1-6 <b>(5)</b>	Dr. Riederer; Dr. Kawashima; Mr. Borisch
Subtask 1.2: Design, construct, and test phantom which mimics geometry for prostate MRI	1-6 <b>(6)</b>	Dr. Riederer; Mr. Hulshizer
Subtask 1.3: Experimentally test and evaluate versions of pulse sequence with prostate phantom and select optimum sequence with standard receiver coil array	6-12 <b>(9,ongoing)</b> <b>(12)</b>	Dr. Riederer; Mr. Hulshizer
Subtask 1.4: Apply initial optimized pulse sequence to three volunteers with standard receiver coil array	13-15 <b>(15)</b>	Dr. Riederer; Dr. Kawashima

Subtask 1.5: Experimentally test and evaluate pulse sequence and triangular array with prostate phantom and select optimum sequence	16-24 <b>(20)</b>	Dr. Riederer; Mr. Hulshizer
Subtask 1.6: Determine parameter options for pulse sequence using prototype triangular coil array	18-24 <b>(20, ongoing)</b>	Dr. Riederer; Mr. Borisch
Subtask 1.7: Apply optimized pulse sequence and triangular coil array in nonrealtime human studies	25-27 <b>(27)</b>	Dr. Riederer; Dr. Kawashima
<i><b>Milestone Achieved:</b> development of accelerated CAPR pulse sequence with 1 mm<sup>3</sup> resolution and 2 sec frame time with triangular coil array</i>		
<b>Specific Aim 2: Development of Special Purpose Receiver Coil Arrays</b>		
Major Task 2: Optimization of pCAPR Pulse Sequence Applied to Prostate Imaging		
Subtask 2.1: Select optimum triangular element size and construct matched single pair of coils	1-6 <b>(3)</b>	Dr. Riederer; Mr. Hulshizer
Subtask 2.2: Construct, tune, and match multiple pairs of triangular coils	7-12 <b>(9)</b>	Dr. Riederer; Mr. Hulshizer
Subtask 2.3: Test modular triangular coil element prototype array with up to 16 elements (8 coil pairs) in experimental phantom studies	13-18 <b>(18)</b>	Dr. Riederer; Mr. Hulshizer
Subtask 2.4: Redesign phase of adjusted coil geometry based on evaluation of prototype triangular coil	28-30 <b>(30)</b>	Dr. Riederer; Mr. Hulshizer
Subtask 2.5: Construct and test revision of triangular-based modular array	31-36 <b>(34)</b>	Dr. Riederer; Mr. Hulshizer
<i><b>Milestone Achieved:</b> development of modular array of triangular-element coils with circumferential placement around pelvis allowing L/R, A/P, and S/I acceleration</i>		
<b>Specific Aim 3: Formation of Optimized pCAPR Images</b>		
Major Task 3.1: Image Reconstruction and System Integration		
Subtask 3.1: Allowance for arbitrary acceleration factors (R <sub>y</sub> , R <sub>z</sub> ) and CAIPIRINHA kernels for arbitrary R	1-6 <b>(6)</b>	Mr. Borisch
Subtask 3.2: Incorporate pCAPR pulse sequence into image reconstruction framework	7-12 <b>(7)</b>	Mr. Borisch
Subtask 3.3: Implement multi-processor execution of individual modules of reconstruction process	12-24 <b>(18)</b>	Mr. Borisch

Subtask 3.4: Perform high speed “real time” image reconstruction of optimized pCAPR pulse sequence, and triangular coil array in phantom studies	24-32 (36)	Mr. Borisch
Subtask 3.5: Test optimized pCAPR pulse sequence, triangular coil array, and realtime reconstruction in human studies	33-36 (36)	Dr. Riederer; Dr. Kawashima; Mr. Borisch
<i><b>Milestone Achieved:</b> development of optimized pulse sequence, triangular coil array and reconstruction providing 1 mm<sup>3</sup> resolution and 2 sec frame times in real time with initial results in patients with prostate cancer</i>		

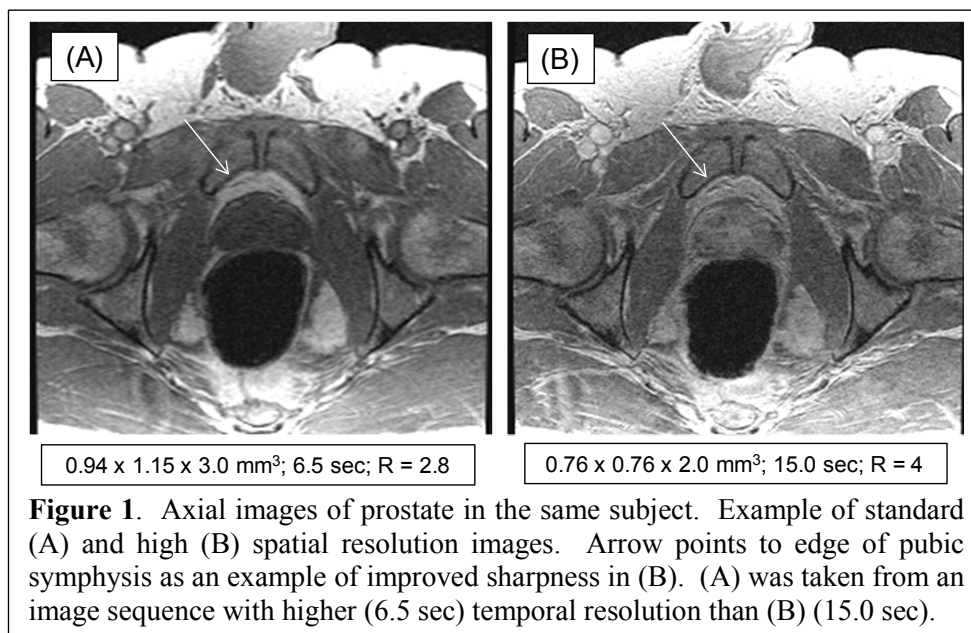
### What was accomplished under these goals?

The grant activities were subdivided into three specific aims with subtasks for each. We have completed the work for all three aims. The following paragraphs are associated with the specific subtasks identified in the Statement of Work (SOW).

#### Specific Aim 1

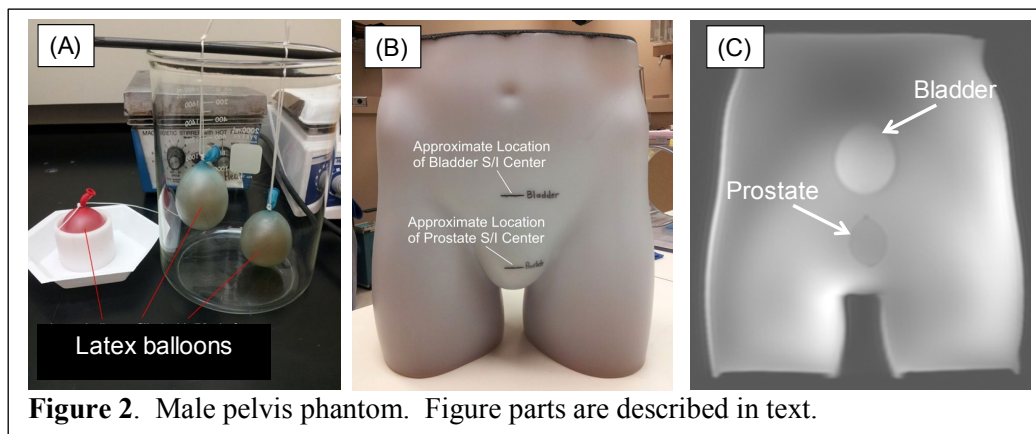
*Subtask 1.1.* For this subtask parameter sets for various combinations of spatial and temporal resolution and acceleration factor (R) were evaluated using g-factor analysis, signal-to-noise ratio (SNR), and radiologist preference. Two target applications of dynamic-contrast-enhanced (DCE) MRI with potentially different spatiotemporal resolution were defined

by our collaborating radiologist. The first application is used to image patients suspected of prostate cancer. In this case “high” temporal resolution of 6-8 sec per image is desired. The second application is for patients who have undergone intervention such as prostatectomy or radiation therapy for prostate cancer but have had subsequent nonzero PSA measurements. For these cases of what is referred to as “biochemical recurrence” high spatial resolution is desired with potentially coarser image update times. G-factor analysis takes images of the sensitivity across the 3D volume of each individual coil element and algebraically computes the level of noise amplification when acceleration is performed. As increased acceleration factors R are used in the acquisition, the resultant SNR deteriorates. Folding these considerations of adequate SNR and target spatiotemporal resolution together, two target working parameter sets have been identified and implemented in baseline acquisitions. The parameter sets are indicated and resultant images illustrated in **Figure 1** for the pre-intervention prostate patient (A) and for the biochemical recurrence application (B). The arrows identify one specific anatomic feature which illustrates the improved spatial resolution in (B).

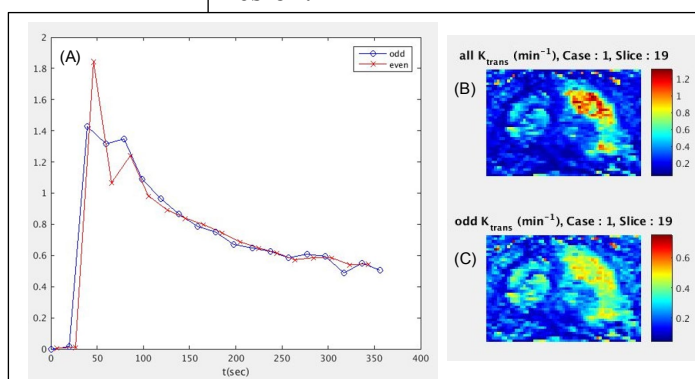
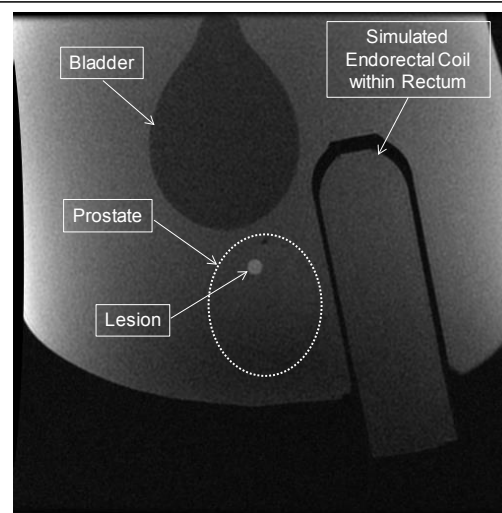


*Subtask 1.2.* For Subtask 1.2 we have designed and constructed a phantom which mimics the male pelvis for MR imaging (**Figure 2**). We started with a plastic shell of the male pelvis which corresponds to a male with BMI of

approximately 25. We wished to incorporate inclusions to simulate both the bladder and the prostate gland. This was done using latex balloons filled with 50 ml of differing B-gel solutions as shown in (A). These balloons were then positioned within the overall plastic shell while it was filled with B-gel, sorbic acid, and NaCl in distilled water. The solution then solidifies. A photograph of the final phantom is shown in (B), with marking showing the locations of the two inclusions. The overall weight is 21.5 kg. We have initiated studies for Subtask 1.3 in which MR images are acquired (e.g. C). Such images were used to aid in selecting the optimum.



*Subtask 1.3.* Work on this subtask continued since the time of the first year progress report. The phantom previously developed was further modified to include several simulated lesions within the inclusion simulating the prostate. A sagittal MR image of the phantom is shown in **Figure 3**. The overall size of the phantom simulates a patient of an approximate BMI of 23. A larger phantom is also being constructed. Related to this we have studied the effect of temporal resolution on the fidelity with which perfusion parameters are estimated. This was done by starting with the data acquired at 6.5 sec frame time and down sampling; i.e. taking every other point or possibly every third point. Results similar to those in **Figure 4** show that temporal sampling coarser than the 6.5 sec used in this work causes underestimation of perfusion parameters.



*Subtask 1.4.* This subtask involved use of the optimized pulse sequence in three volunteers using the standard receiver coil array. The principal target group of patients is that which is “treatment-naïve” in that prostate cancer is suspected but the presence or degree of disease must be determined

prior to determination of possible treatment. The optimum sequence was identified in the first year, and for such patients temporal sampling the realm of 5 to 7 seconds represented a good tradeoff between spatial and temporal resolution. Volunteers have been imaged using the standard 12-element receiver coil array, and in fact this has been expanded to include studies of patients who are referred for prostate MRI. Further, we have studied to possible extension of the acquisition to include more, specifically 32, of the multicoil elements available. These additional elements are generally positioned more laterally than the reference 12 elements. For the same scan, use of 32 elements consistently provides improved image quality. Sample results are shown in **Figure 5**, and we have published these finding.

*Subtask 1.5.* For this task we used a 12-element array composed of the new triangular elements and imaged a prostate phantom to assess performance using the target prostate perfusion pulse sequence. Sample results are shown in **Figure 6**. This figure shows maximum intensity projection (MIP) images of the g-factor, a measure of the noise amplification of the coil array for sagittal (A), coronal (B) and axial (C) orientations. Also shown in (D) is the cumulative g-factor as measured over the 3D volume being imaged. Based on this work, we selected this acceleration combination, which with TR 5.3 msec provides the optimum sequence with 6.5 sec time resolution with  $256 \times 384 \times 38$  spatial resolution.

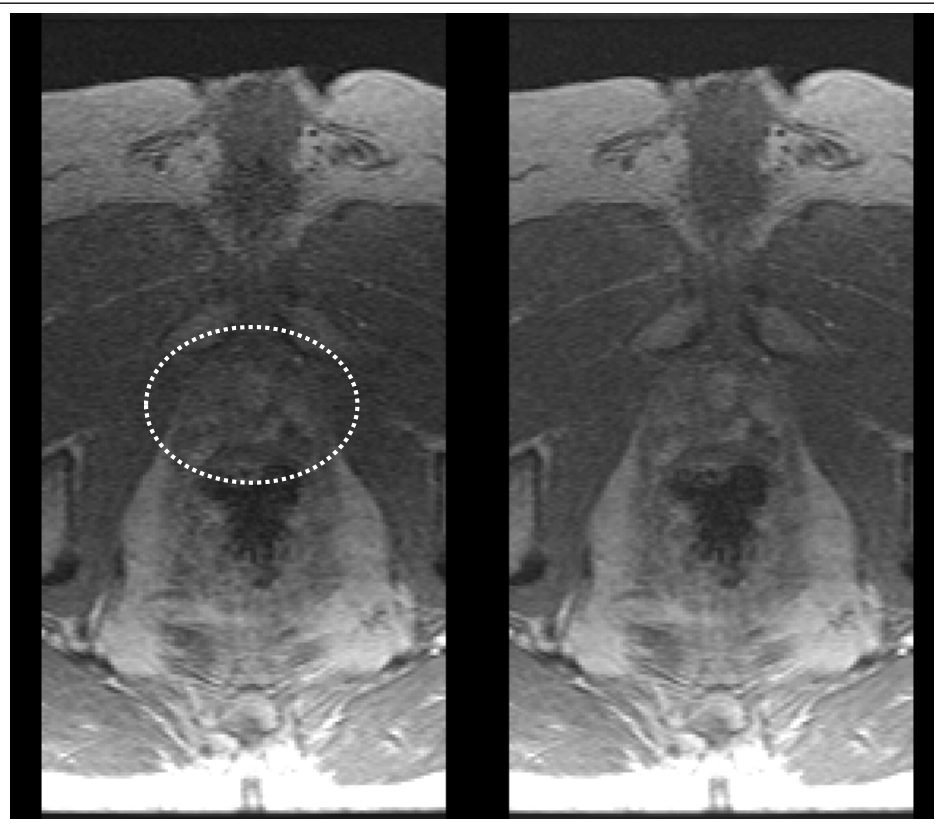


**Figure 5.** Comparison of images of the prostate acquired using 12-element standard coil (left) and 32-element coil (right). Prostate is identified within the dashed ellipse. The right image has superior signal-to-noise ratio.

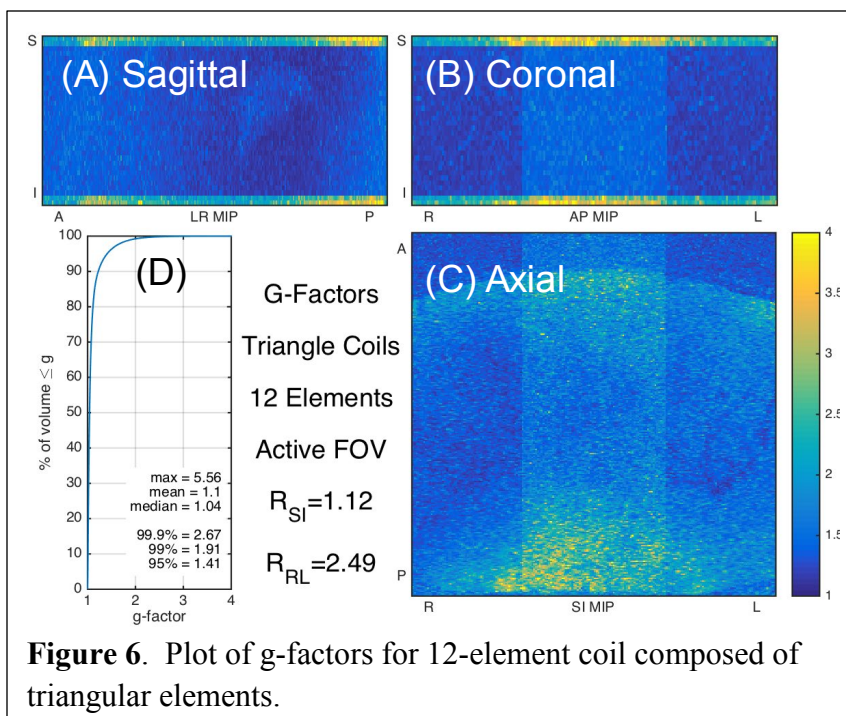


**Figure 6.** Plot of g-factors for 12-element coil composed of triangular elements.

Based on this work, we selected this acceleration combination, which with TR 5.3 msec provides the optimum sequence with 6.5 sec time resolution with  $256 \times 384 \times 38$  spatial resolution.

*Subtask 1.6.* In the progress report from 2017 we presented data showing that temporal resolution inferior to 6.5 sec update times can cause underestimation of quantitative parameters such as  $K_{trms}$  which are used to characterize the behavior of the DCE-MRI signal as contrast material perfuses through the prostate gland. We have studied this phenomenon in work going beyond that initially proposed in the grant application by developing a new algorithm for quantitative modeling of the DCE-MRI data. It uses the variable projection or “Varpro” technique to modify the process of estimating multiple variables (in this case the volume transfer constant  $K_{trms}$  and the rate constant  $k_{ep}$ , both measured in  $\text{min}^{-1}$ ) in parallel into separate one-dimensional estimation processes. We have found that this works effectively for prostate DCE-MRI, as it more reliably converges to a solution using the DCE-MRI data set and provides some improvement in speed in the estimation process. We have recently published this work in the refereed literature in the journal article by Kargar as indicated later in this report. The material in **Figure 7** illustrates this method, showing how the minimum of a cost function can be determined from the DCE-MRI data for a cancerous region (A) and a normal region (B) of the prostate. The curves in (C) show acquired DCE-MRI data in the jagged curves and the estimates made using the fitted parameters resulting from this algorithm as dashed curves. A clinical example of the use of the Varpro technique in a patient with prostate cancer is shown in **Figure 8**. Here the lesion is well seen in the ADC map (B, arrow), but is further well characterized in the elevated  $K_{trms}$  and  $k_{ep}$  values (C, D). Further details are provided in the journal article by Kargar et al provided in the Appendix.

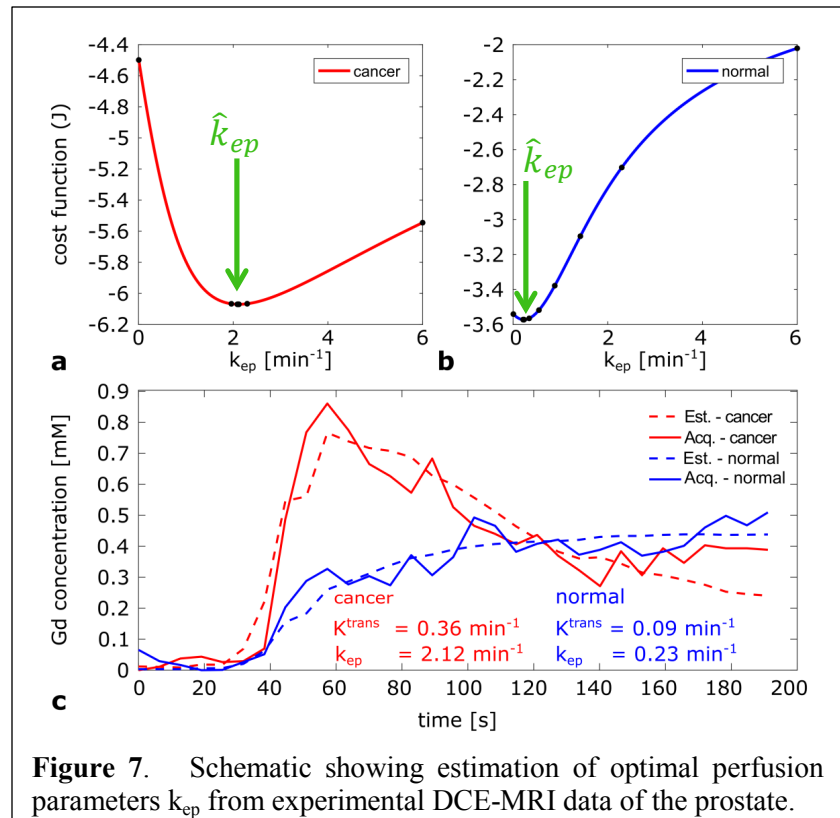


**Figure 7.** Schematic showing estimation of optimal perfusion parameters  $k_{ep}$  from experimental DCE-MRI data of the prostate.

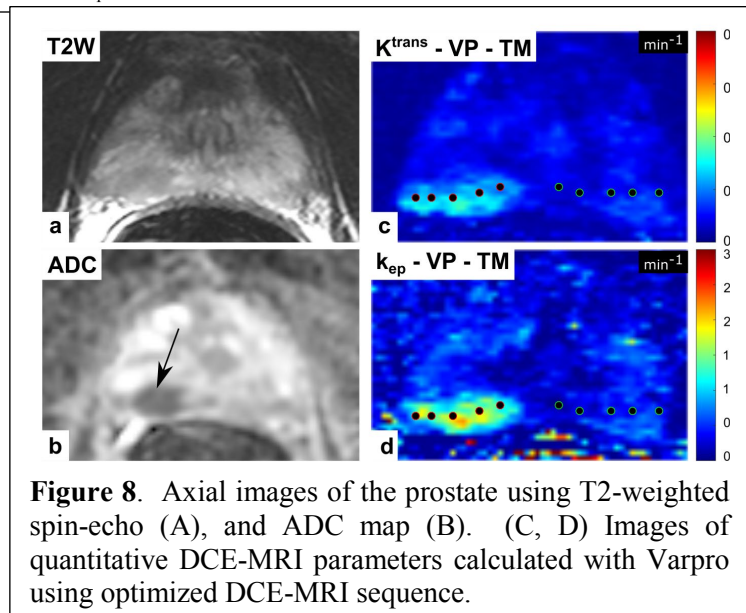
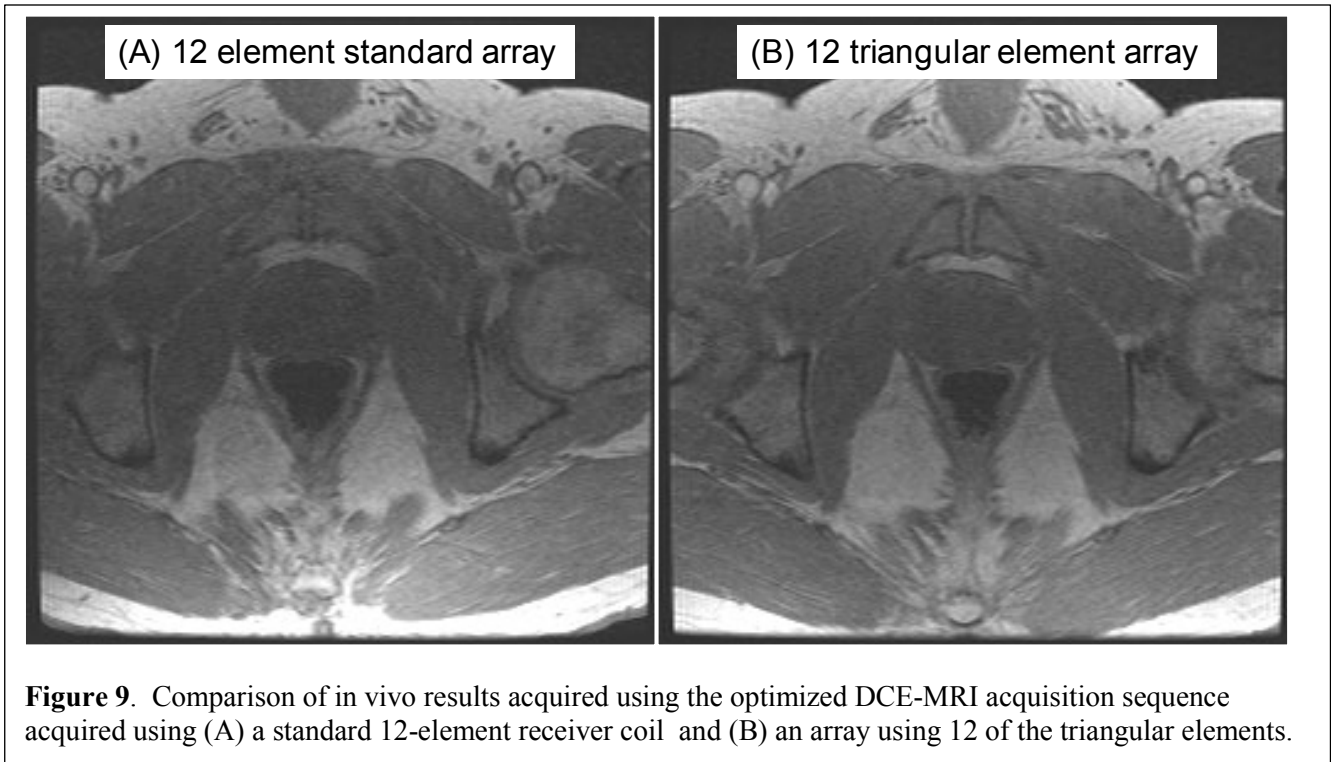


**Figure 8.** Axial images of the prostate using T2-weighted spin-echo (A), and ADC map (B). (C, D) Images of quantitative DCE-MRI parameters calculated with Varpro using optimized DCE-MRI sequence.

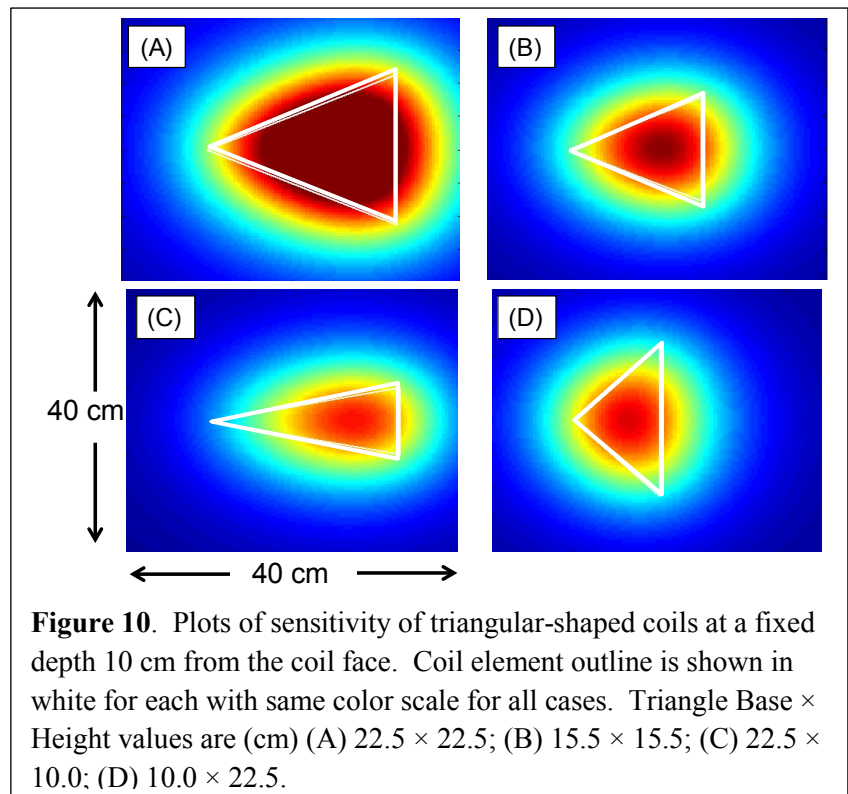
*Subtask 1.7.* The final task of Specific Aim 1 was to apply the optimized pulse sequence and triangular coil arrays in non-realtime imaging of humans. This has been accomplished. Results from human studies are presented in **Figure 9**. Shown are axial images of a male subject at a level through the prostate. These are individual images from a 3D image set acquired with the DCE-MRI sequence



as studied in Specific Aim #1. Shown are the result (A) using the standard 12-element phased array which is embedded within the patient table. This is compared with a separate scan performed on the same subject but using the newly developed array with 12 triangular elements for signal reception. The overall image quality is very similar for both results. The result using the triangular elements (B) has an approximate 20% improvement in the visual SNR in the region of the prostate. We are very pleased with these results.

### Specific Aim 2

*Subtask 2.1.* For Subtask 2.1 we evaluated a variety of triangular coil elements with different apex angles and sizes using simulations based on the Biot-Savart Law as well as experimental measurements of sensitivity. Sample results of a simulation are shown in **Figure 10A**. This shows the sensitivity across a plane at a depth of 10 cm from an assumed triangular element with each element shown as the white outline. As desired, the sensitivity varies along the x-direction of the plot (left-right for these), corresponding to the superior-inferior (S/I) direction for a patient. From results like this the coil element in (A) was large enough to have adequate



sensitivity at depth and had adequate variation of sensitivity along the x-direction. This element (22.5 cm base  $\times$  22.5 cm height) was chosen for further study. Use of the sensitivity data from a single coil was then replicated at assumed coil locations and then used together to synthesize multi-coil acquisition. From this information g-factor maps were calculated. Based on results to minimize g-factor for acceleration factors no higher than about  $R = 4$  as well as consideration of the need to image a S/I field of view of 10 cm or more to encompass the prostate, this coil element size was chosen for construction.

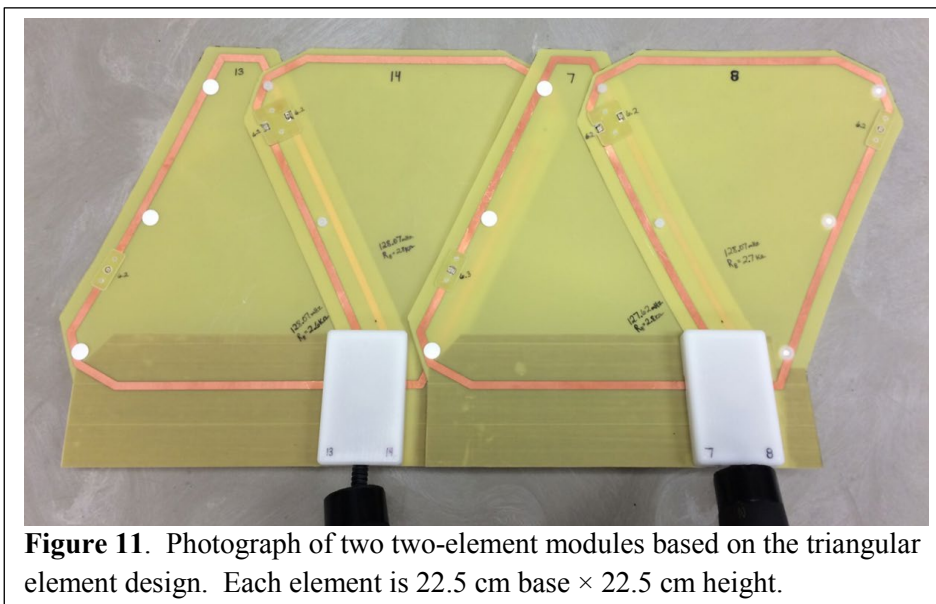


**Figure 11.** Photograph of two two-element modules based on the triangular element design. Each element is 22.5 cm base  $\times$  22.5 cm height.

#### *Subtask 2.2.*

For Subtask 2.2 two pairs of elements, four elements total, of this target size were constructed. Use of such paired modules allows patient-specific selection of the number of modules as based on patient size. Two such modules are shown in **Figure 11**. This was further studied during the subsequent year. Part of this study will be to compare performance of the proposed triangular-element-based array with other multi-element arrays.

#### *Subtask 2.3.*

The results in Figure 11 show two two-element coils. As specified in this subtask, we have further constructed a 16-element coil composed of the triangular elements. The design using two-element modules allows the total number of elements to be matched to the body habitus, i.e. patient diameter. A photograph of the 16-element coil is shown in **Figure 12**.

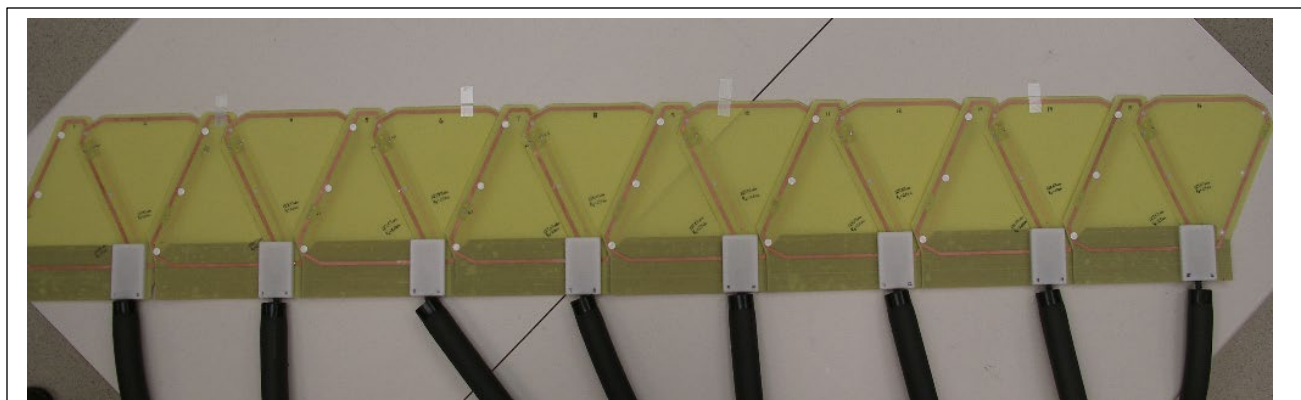
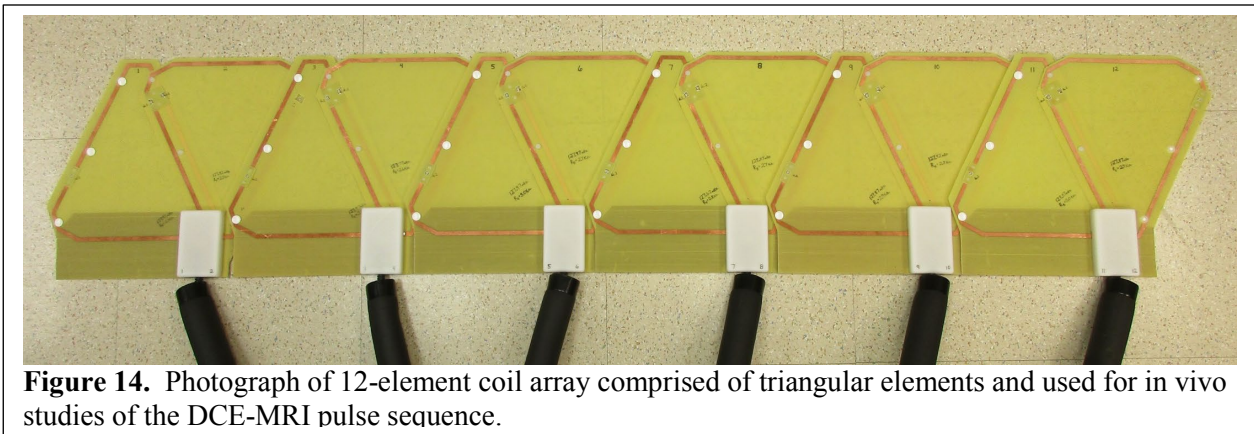
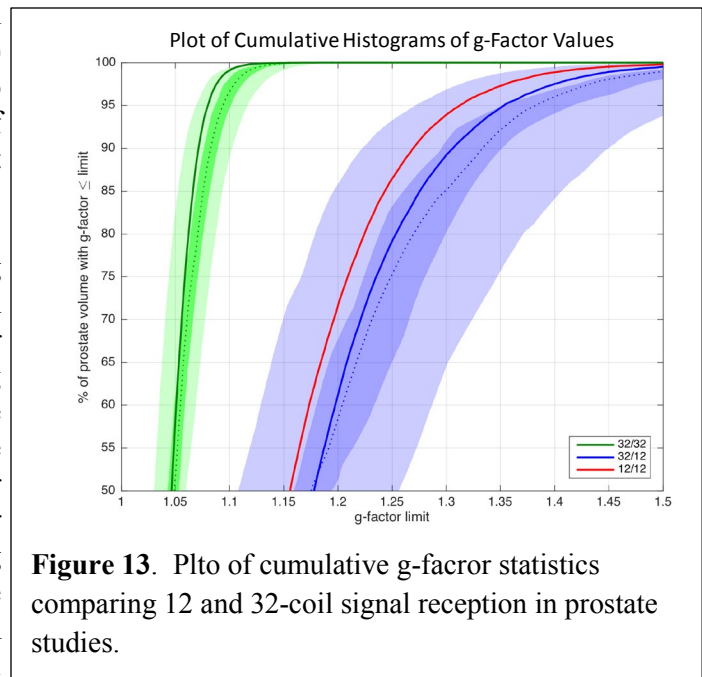


**Figure 12.** Photograph of 16-element coil composed of triangular elements.

*Subtask 2.4.* In a continuation of work initiated and reported in Year 2, comparisons of performance of the triangular-element coil array and 12- and 32-element standard arrays were done. Specifically, the coil arrays were compared on the basis of the ability to retain signal-to-noise ratio (SNR) in accelerated scans. This is done using the “geometry” or “g-factor.” Sample results are shown in **Figure 13** for two-dimensional SENSE acceleration  $R=3.35$ , typical for what is allowable in prostate

imaging. Here the left-right (L/R) acceleration is 3.00, and the superior-inferior (S/I) acceleration is 1.12, the product of the two resulting in 3.35. The superiority of performance of the 32-element array is due not only to the use of more elements (32 vs. 12), but also to the ability to position the elements more laterally about the patient, allowing improved (reduced) g-factors for the L/R acceleration. These results led us to reconsider the design of an adjusted coil geometry having 16 elements. However, for elements of the same size this necessarily causes the circumference of the array to be much larger than the typical prostate patient. On the other hand, accommodating 16 elements by reducing the element size necessarily causes a decrease in performance due to the rapid falloff of SNR with depth. Thus, the 12-element coil comprised of 22.5 cm x 22.5 cm height triangles is optimum for this configuration when placed circumferentially around the patient.



*Subtask 2.5.* This subtask of construction of the optimum coil array was performed. A photograph of the 12-element array is shown in **Figure 14**.

### Specific Aim 3

#### *Subtask 3.1.*

For Subtask 3.1 we have modified our reconstruction software to allow for arbitrary acceleration factors and kernels as desired. Examples of this were shown previously in Figure 1 in which the image in (A) was reconstructed using SENSE acceleration  $R = R_Y \times R_Z = 2.50 \times 1.12 = 2.80$  while that in (B) used  $R = 3.56 \times 1.27 = 4.17$ .

#### *Subtask 3.2.*

For Subtask 3.2 we have installed the basic dynamic contrast-enhanced (DCE-MRI) pulse sequence based on our CAPR k-space sampling onto several GE 3.0 Tesla MRI scanners and developed the software to direct the acquired MRI data to our custom computation hardware for online reconstruction. This allows rapid reconstruction of scans made of phantoms or of human subjects originating from

multiple MRI scanners across Mayo.

### Subtask 3.3.

The reconstruction hardware was identified last year, further developed and is shown schematically in **Figure 15**. We have made progress on this aim and have updated the hardware to include two CPU packages, each with 14 physical cores and 28 threads, and thus a total of 28 cores (processor elements) and 56 threads. This routinely allows fast, clinically acceptable reconstruction times of 3D time-resolved, multi-coil (32 element) accelerated images of dynamic-contrast-enhanced (DCE) MRI. Each of the steps in the reconstruction comprises an individual module.

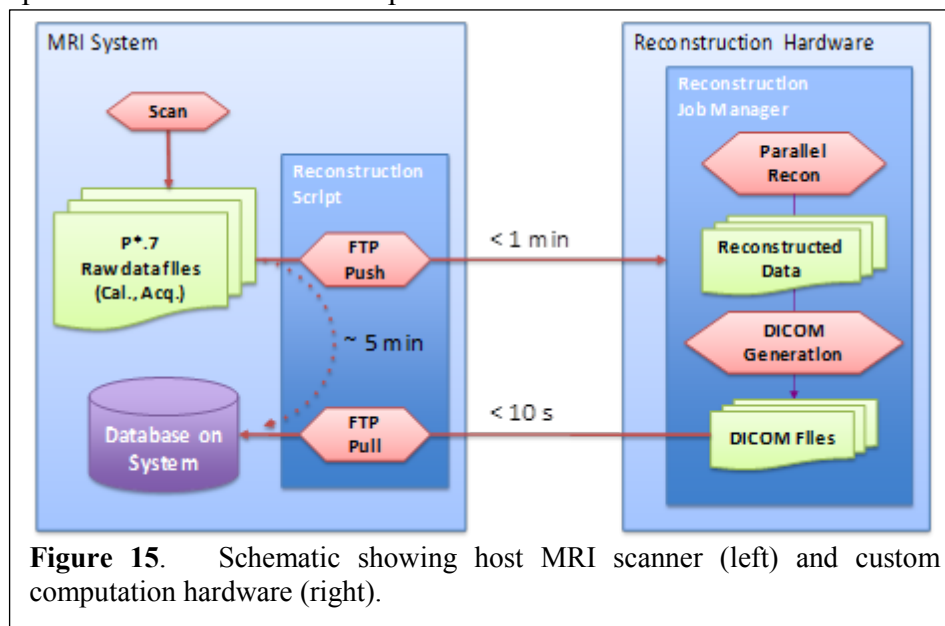


**Figure 15.** Schematic showing host MRI scanner (left) and custom computation hardware (right).

### Subtask 3.4.

We have applied the reconstruction hardware developed previously to studies in phantoms performed using the triangular coil arrays. The time to reconstruct approximately 40 3D high resolution (220 x 440 x 122 sampling resolution) time frames is approximately one minute. These reconstructed images are passed back to the native MRI scanner on which the acquisition was done and are made available for viewing within this time.

### Subtask 3.5.

We have also used the reconstruction hardware in human studies with the optimized pulse sequence and the triangular coil array. Results presented in Figure 9 were reconstructed using this. We also note that this reconstruction apparatus has been interfaced directly into the clinical MRI practice at Mayo Clinic Rochester. It can be used with arbitrary receiver coil arrays and is not limited to the triangular element arrays which were the focus of this grant. This is currently used for the DCE-MRI pulse sequence which is a standard component of the multi-parameter prostate MRI exam of treatment-naïve subjects in whom the presence of prostate cancer is to be determined. In our clinical practice this sequence and the associated high speed reconstruction are used in approximately 11 patient exams per day. At the request of our colleagues in the clinical MRI practice at Mayo Clinic Arizona we have also assembled a clone of this reconstruction hardware and installed it within at the Mayo Hospital in Phoenix, Arizona. Since the time of installation there this technology has been used in over 100 patient studies at that site.

**What opportunities for training and professional development has the project provided?**

Nothing to report.

**How were the results disseminated to communities of interest?**

Nothing to report other than that in Section 6 of this report.

**What do you plan to do during the next reporting period to accomplish the goals?**

This is the Final Report of this grant.

4. **IMPACT:** Describe distinctive contributions, major accomplishments, innovations, successes, or any change in practice or behavior that has come about as a result of the project relative to:

**What was the impact on the development of the principal discipline(s) of the project?**

The tasks completed in this three-year project provide a good basis for future work in the areas of study.

**What was the impact on other disciplines?**

Nothing to Report

**What was the impact on technology transfer?**

Our baseline DCE-MRI pulse sequences are now used clinically at Mayo Clinic, both in Rochester and at Mayo Clinic Arizona. This is approximately 11 patient studies per day.

**What was the impact on society beyond science and technology?**

Nothing to Report

5. **CHANGES/PROBLEMS:** The PD/PI is reminded that the recipient organization is required to obtain prior written approval from the awarding agency grants official whenever there are significant changes in the project or its direction. If not previously reported in writing, provide the following additional information or state, "Nothing to Report," if applicable:

**Changes in approach and reasons for change**

Nothing to Report

**Actual or anticipated problems or delays and actions or plans to resolve them**

Nothing to Report

**Changes that had a significant impact on expenditures**

Nothing to Report

**Significant changes in use or care of human subjects, vertebrate animals, biohazards, and/or select agents****Significant changes in use or care of human subjects**

Nothing to Report

**Significant changes in use or care of vertebrate animals**

Nothing to Report

**Significant changes in use of biohazards and/or select agents**

Nothing to Report

**6. PRODUCTS:** List any products resulting from the project during the reporting period. If there is nothing to report under a particular item, state “Nothing to Report.”

- **Publications, conference papers, and presentations**

Report only the major publication(s) resulting from the work under this award.

**Journal publications.**

1. Riederer SJ, Borisch EA, Froemming AT, Grimm RC, Kawashima A, Mynderse LA, Trzasko JD, “Improved performance of prostate DCE-MRI using a 32-coil vs. 12-coil receiver array.” *Magn Reson Imaging* 39:15-23 (2017).
2. Kargar S, Borisch EA, Froemming AT, Kawashima A, Mynderse LA, Stinson EG, Trzasko JD, Riederer SJ, “Robust and efficient pharmacokinetic parameter estimation for dynamic contrast enhanced MRI of the prostate.” *Magn Reson Imaging* 48:50-61 (2018).

**Books or other non-periodical, one-time publications.**

Nothing to Report

### Other publications, conference papers and presentations.

1. Kargar S, Stinson EG, Borisch EA, Froemming AT, Kawashima A, Mynderse LA, Trzasko JD, Riederer SJ, "Robust and efficient estimation of optimum perfusion parameters in dynamic contrast-enhanced MRI of the prostate." 27th Annual Intl Conf on Magnetic Resonance Angiography, Cincinnati OH, Sept16-18, 2015.
2. Riederer SJ, Borisch EA, Froemming AT, Grimm RC, Kawashima A, Trzasko JD, "Improved SNR performance of prostate DCE-MRI using 32 receiver channels." Radiol Soc North America, Chicago IL, Nov 2015. PH251-SD-TUB5.
3. Kargar S, Stinson EG, Borisch EA, Froemming AT, Kawashima A, Mynderse LA, Trzasko JD, Riederer SJ, "An efficient variable projection strategy for pharmacokinetic parameter estimation inf prostate DCE-MRI." ISMRM Workshop on Data Sampling, Sedona AZ, January 10-14, 2016.
4. Riederer SJ, Borisch EA, Froemming AT, Grimm RC, Kawashima A, Trzasko JD, "Prostate DCE-MRI: improved SNR with 32-element receiver arrays." Annual Mtg Europ Cong Radiol, Vienna Austria, March 2-6, 2016.
5. Trzasko JD, Borisch EA, Froemming AT, Kawashima A, Warndahl BA, Grimm RC, Mynderse LA, Young PM, King BF, Stinson EG, Manduca A, Riederer SJ, "Sparse reconstruction of 4D prostate DCE-MRI: integration into routine clinical practice." Int'l Symp on Biomedical Imaging, Prague, Czech Republic, April 13-16, 2016.
7. Kargar S, Stinson EG, Borisch EA, Froemming AT, Kawashima A, Mynderse LA, Trzasko JD, Riederer SJ, "Patient-specific vs. population-based arterial input function in perfusion estimation for DCE-MRI of the prostate." Presented at 28<sup>th</sup> Annual Meeting of Society of Magnetic Resonance Angiography, Chicago IL, September 2016.
8. Kargar S, Borisch EA, Froemming AT, Kawashima A, Mynderse LA, Stinson EG, Trzasko JD, Riederer SJ, "Robust and efficient pharmacokinetic parameter estimation for dynamic contrast enhanced MRI of the prostate." Presented at 24<sup>th</sup> Annual Meeting, ISMRM, Honolulu HI, April 2017.

- **Website(s) or other Internet site(s)**

Nothing to Report

- **Technologies or techniques**

Nothing to Report

- **Inventions, patent applications, and/or licenses**

Nothing to Report

- **Other Products**

Nothing to Report

## 7. PARTICIPANTS & OTHER COLLABORATING ORGANIZATIONS

### What individuals have worked on the project?

Name:	Stephen J. Riederer, Ph.D.
Project Role:	Principal Investigator
Nearest person month worked:	1.8
Contribution to Project:	Dr. Riederer directs all technical aspects of the projects.

Name: Akira Kawashima, M.D., Ph.D.  
 Project Role: Co-Investigator  
 Nearest person month worked: .22  
 Contribution to Project: Dr. Kawashima oversees feasibility testing performed in volunteers and provides feedback on intermediate results for all projects.

Name: Eric A. Borisch  
 Project Role: Information Services Technical Specialist  
 Nearest person month worked: 2.76  
 Contribution to Project: Mr. Borisch is responsible for writing and developing production-level software for all projects, software heavily centered on reconstruction of 2D-accelerated 3D data sets acquired with various view orders.

Name: Thomas C. Hulshizer  
 Project Role: MR Technician  
 Nearest person month worked: 1.2  
 Contribution to Project: Mr. Hulshizer is responsible for construction of the pelvis-prostate phantom, construction and tuning of RF coils, and testing of prototype MR pulse sequences using phantoms.

**Has there been a change in the active other support of the PD/PI(s) or senior/key personnel since the last reporting period?**

In August 2018 support for the PI at a level of 25% was started from the Mayo Clinic Discovery-Translation program for the project “Advanced MRI Acquisition and Reconstruction for High Resolution Prostate MRI.” This did not alter his level of effort for this CDMRP grant.

**What other organizations were involved as partners?**

Nothing to Report other than the general support provided by the PI’s institution, Mayo Clinic.

**8. SPECIAL REPORTING REQUIREMENTS**

None

- 9. APPENDICES:** Attach all appendices that contain information that supplements, clarifies or supports the text. Examples include original copies of journal articles, reprints of manuscripts and abstracts, a curriculum vitae, patent applications, study questionnaires, and surveys, etc.

**Journal Articles**

Attached is a pdf version of each of the two journal publications indicated in Section 6 above.



Original contribution

## Improved performance of prostate DCE-MRI using a 32-coil vs. 12-coil receiver array



Stephen J. Riederer<sup>a,\*</sup>, Eric A. Borisch<sup>a</sup>, Adam T. Froemming<sup>a</sup>, Roger C. Grimm<sup>a</sup>, Akira Kawashima<sup>c</sup>, Lance A. Mynderse<sup>b</sup>, Joshua D. Trzasko<sup>a</sup>

<sup>a</sup> Department of Radiology, Mayo Clinic, 200 First Street SW, Rochester, MN 55905, United States

<sup>b</sup> Department of Urology, Mayo Clinic, 200 First Street SW, Rochester, MN 55905, United States

<sup>c</sup> Department of Radiology, Mayo Clinic, 13400 E. Shea Blvd., Scottsdale, AZ 85259, United States

### ARTICLE INFO

#### Article history:

Received 3 September 2016

Received in revised form 24 January 2017

Accepted 24 January 2017

#### Keywords:

Prostate MRI

DCE-MRI

Multi-element receiver coil

### ABSTRACT

**Purpose:** To assess whether acquisition with 32 receiver coils rather than the vendor-recommended 12 coils provides significantly improved performance in 3D dynamic contrast-enhanced MRI (DCE-MRI) of the prostate.

**Materials:** The study was approved by the institutional review board and was compliant with HIPAA. 50 consecutive male patients in whom prostate MRI was clinically indicated were prospectively imaged in March 2015 with an accelerated DCE-MRI sequence in which image reconstruction was performed using 12 and 32 coil elements. The two reconstructions were compared quantitatively and qualitatively. The first was done using signal-to-noise ratio (SNR) and g-factor analysis to assess sensitivity to acceleration. The second was done using a five-point scale by two experienced radiologists using criteria of perceived SNR, artifact, sharpness, and overall preference. Significance was assessed with the Wilcoxon signed rank test. Extension to T2-weighted spin-echo and diffusion sequences was assessed in phantom studies.

**Results:** Reconstruction using 32 vs. 12 coil elements provided improved performance in DCE-MRI based on intrinsic SNR (18% higher) and g-factor statistics (14% higher), with a median 32% higher overall SNR within the prostate volume over all subjects. Reconstruction using 32 coils was qualitatively rated significantly improved ( $p < 0.001$ ) vs. 12 coils on the basis of perceived SNR and radiologist preference and equivalent for sharpness and artifact. Phantom studies suggested the improvement in intrinsic SNR could extend to T2-weighted spin-echo and diffusion sequences.

**Conclusions:** Reconstruction of 3D accelerated DCE-MRI studies of the prostate using 32 independent receiver coils provides improved overall performance vs. using 12 coils.

© 2017 Elsevier Inc. All rights reserved.

## 1. Introduction

MR imaging of the prostate is commonly performed using a multi-parametric approach in which multiple sequences are used to aid in radiologic interpretation [1–3]. In addition to T2-weighted spin-echo (T2SE) and diffusion-weighted image (DWI) a pulse sequence typically used within this exam is three-dimensional (3D) dynamic contrast-enhanced MRI (DCE-MRI) [4–6] in which a contrast agent is administered intravenously, and images are acquired of the prostate to observe washin and washout of the contrast-enhanced blood over the entire prostate volume. DCE-MRI continues to be used in the context of the PI-RADS version 2 reporting system for prostate cancer for treatment-

naïve prostate glands [7]. Further, recurrence of prostate cancer after definitive treatment has been reported to be in the 15 to 40% range [8, 9], and in such cases DCE-MRI has been shown to be of high value [10, 11]. Because the desired spatiotemporal resolution of the DCE-MRI sequence typically pushes the limits of signal-to-noise ratio (SNR), the need for good performance of the receiver coils is important [12].

For prostate MRI the coil usage reported in the literature is highly variable. One significant choice is whether an endorectal (ER) coil should be used, and several studies have compared ER with non-ER acquisition [13–16]. However, whether an ER coil is used or not, in contemporary prostate MRI some kind of multi-element receiver coil is generally used. A sampling of the recent literature shows use of multi-element coils having four [17], six [18], eight [11,15,19], 12 to 15 [6], and 18 [20] elements, or with the number of elements not explicitly given [4,5].

For many contemporary MRI systems the number of receiver channels available is 32 or more. Also, coil arrays with literally dozens of elements are now embedded within the patient table. Although both of these factors can greatly facilitate the usage of a large number of elements for a

\* Corresponding author.

E-mail addresses: [riederer@mayo.edu](mailto:riederer@mayo.edu) (S.J. Riederer), [borisch.eric@mayo.edu](mailto:borisch.eric@mayo.edu) (E.A. Borisch), [Froemming.Adam@mayo.edu](mailto:Froemming.Adam@mayo.edu) (A.T. Froemming), [Grimm.Roger@mayo.edu](mailto:Grimm.Roger@mayo.edu) (R.C. Grimm), [Kawashima.Akira@mayo.edu](mailto:Kawashima.Akira@mayo.edu) (A. Kawashima), [Mynderse.Lance@mayo.edu](mailto:Mynderse.Lance@mayo.edu) (L.A. Mynderse), [Trzasko.Joshua@mayo.edu](mailto:Trzasko.Joshua@mayo.edu) (J.D. Trzasko).

given exam, it is not clear what the number or combination of elements should be for prostate MRI. If an ER coil is not used, then it is important to have a multicoil setup which provides high SNR in the region of the prostate. The results of Ref. [16] indicated superior performance for the combination of an ER coil and a 16-element multicoil vs. use of a six-element multicoil alone. However, separation of the improvement due to the change of the multicoil vs. use of the ER coil was not determined.

Prostate MRI at our institution is principally performed using a wide-bore 3 T MRI system with features similar to those described above. The vendor-recommended, default coil selection for prostate DCE-MRI calls for 12 channels of data acquisition to be used of the 32 available on the system. These 12 channels include eight active elements from the array contained within the table posterior to the supine patient and four active elements used from a 16-element array placed anteriorly. In investigating to what extent the DCE-MRI sequence could be accelerated, we considered whether additional coil elements could be used. To fully exploit the capability of the MRI system, the option for use of all 32 channels was considered. Thus, the specific hypothesis of this work was that the use of 32 vs. 12 independent receiver coils would provide improved performance in DCE-MRI of the prostate. The feasibility of improved performance for other sequences of a multi-parametric prostate MRI exam was also assessed with phantom studies.

## 2. Materials and methods

This study was approved by the institutional review board which waived the need for written consent. The study was compliant with HIPAA.

### 2.1. Subjects

50 consecutive male subjects for whom a prostate MRI exam was clinically indicated and who gave their assent for their exam results to be used for research purposes were prospectively enrolled in the study over the period March 10–27, 2015. The age, weight, and body mass index (BMI) ranges were 51 to 86 years, 63.5 to 155.1 kg, and 22.5 to 46.8, respectively. Forty-four of the 50 had intact prostates; six were evaluated post-prostatectomy. Other information on the patient cohort, including radiological interpretation, is shown in Table 1. Of note is that 34% (17/50) of the patients were imaged as followup to previous treatment for prostate cancer.

### 2.2. MRI acquisition

All studies were performed on either of two identical 3.0 T MRI scanners (Discovery MR750w, GE Healthcare, Waukesha WI) utilizing an institutional clinical exam protocol. Each machine has a 70 cm diameter bore, a vendor-provided 40-element receiver coil array (Geometry Embracing Method “GEM” array) embedded within the patient table, and 32 receiver channels. Each patient exam included a localizer, T2-weighted spin-echo, and diffusion-weighted sequences, followed by a DCE-MRI study performed with intravenous contrast administration.

Details of the RF-spoiled gradient echo DCE-MRI sequence are shown in Table 2. Contrast material (Dotarem, Guerbet, Paris, France) was administered into an arm vein at a rate of 3 ml/s followed by a 20 ml saline flush at 3 ml/s. The contrast dose was 0.1 mmol/kg, with a maximum of 20 ml for patients weighing 100 kg or more.

The impetus for this study was to push the acceleration of the DCE-MRI sequence for improved spatiotemporal resolution. The sequence used is based on one developed for time-resolved contrast-enhanced MR angiography (CE-MRA) using two-dimensional (2D) SENSE acceleration [21] and view sharing [22]. For this work the slab orientation was approximately axial but with slight forward tilting to align the slab select direction with the central axis of the prostate gland as determined in the sagittal localizer. SENSE acceleration factors of 2.49 and 1.12 were applied along the left/right (L/R) phase encode and approximate superior/inferior (S/I) slice encode directions, respectively, yielding a net acceleration factor of  $R = 2.78$ . DCE-MRI acquisition was initiated 20 s prior to the start of contrast injection, the frame time was approximately 6.6 s, and a total of 33 time frames were collected. Versions of the sequence with higher accelerations were considered for shorter frame times; e.g.  $R = 5.0$  for 4.0 s frame time, but for the same spatial resolution the SNR loss was considered too severe.

### 2.3. Selection of receiver coil elements

This work made use of the 40-element GEM receiver coil array shown schematically in Fig. 1A with a male torso and prostate shown approximately to scale. The array consists of five columns of elements oriented longitudinally within the patient table which for the supine patient are located posteriorly. Also used was a 16-element coil array placed anteriorly consisting of four longitudinally oriented columns each comprised of four elements (Fig. 1B). In both figures an approximate 75 cm<sup>3</sup> sphere, simulating the prostate gland, is shown in red to give a sense of scale of typical gland size to extent of coil coverage.

The combinations of coil elements available for usage are limited by the vendor, and recommendations are made according to the type of exam. For prostate MRI this calls for 12 active receiver coil elements, eight from the GEM array and four from the anterior array. These are highlighted in yellow in Figs. 1A and B, respectively. The elements selected from the GEM array (A) are the two central-most elements which encompass the S/I extent of the prostate, as identified from the sagittal scout images, and the three elements from the next closest columns on each side. For the anterior coil (B) the two central elements from the two rows which similarly encompass the S/I extent of the prostate are selected. All other coil elements from both arrays are electronically disabled during acquisition, and data from the 12 elements are individually digitized and used in reconstruction.

To attempt to exploit the full 32-channel capability of the MRI systems for accelerated DCE-MRI, we next considered use of the vendor-allowed 16 elements from each array. This is also depicted in Figs. 1A–B. Coil elements used for the 12-element case were expanded to include those shown in blue. For the GEM coil (A) the two central-most elements best aligned with the S/I prostate extent are selected as before.

**Table 1**

Summary of patient information and radiological interpretation. Interpretation was based on the full multi-parametric MRI exam, not just the DCE-MRI sequence.

Patients with no prior treatment	Number	Interpretation: no suspicion of significant prostate cancer	Interpretation: suspicion of significant prostate cancer
	33	16	17
Patients with prior treatment	Number	Interpretation: no worrisome lesion	Interpretation: worrisome lesion
Radical prostatectomy	6	2	4
Radiation therapy (external beam or brachytherapy, including with possible adjuvant hormonal therapy)	10	2	8
Hormonal therapy only	1	0	1
Total (patients with prior treatment)	17	4	13
Total (all patients)	50	20	30

**Table 2**

Parameters for 3D RF-spoiled gradient echo prostate DCE-MRI sequence. Acquisition of coil calibration images used the same sequence applied once with phase resolution reduced from 384 to 192.

Parameter	Value
Repetition time (TR)	5.3 msec
Echo time (TE)	2.2 msec
<sup>a</sup> Field of view	220 × 440 × 114 mm <sup>3</sup>
<sup>a</sup> Sampling resolution	256 × 384 × 38
<sup>a</sup> Spatial resolution	0.86 × 1.15 × 3.0 mm <sup>3</sup>
Acceleration	2.49 (R <sub>V</sub> ) × 1.12 (R <sub>Z</sub> ) = 2.78
Frame time	6.6 s
Temporal footprint	≈ 19 s
Number of frames	33
Scan time	≈ 3.5 min

<sup>a</sup> These parameters are all expressed as (frequency × phase × slice) = (A/P × L/R × S/I).

The lateral rows containing those elements are supplemented with the rows of elements next positioned superiorly and inferiorly. For each row the leftmost and rightmost elements (e.g. elements 6 and 36 of Fig. 1A) are automatically combined in vendor hardware prior to digitization, in effect forming one virtual coil from two coil elements. Thus, the 20 elements contained within the four selected rows of the GEM coil are encoded in 16 individual coils, with four of these being two-element combinations. For the anterior array all 16 elements are used (B). It is noted that the channels used for the 12-coil acquisition are a subset of those used for the 32-coil reconstruction. The remaining 20 coil elements located at the ends of the GEM array are electronically disabled during the 32-coil acquisition.

#### 2.4. Image reconstruction

Reconstruction was performed offline with standard SENSE unfolding [23] using a custom-built computing system described in [24]. To avoid the complications and potential variability of performing two separate DCE-MRI studies on each subject, we investigated if a single 32-coil acquisition could be done and the 12-coil acquisition accurately simulated by using only the appropriate 12 data sets for reconstruction. The risk with this approach is that the electronically active but unused 20 coil elements in the 32-active-element acquisition would interfere through undesirable coupling with the 12 elements selected for reconstruction. To assess this we first performed test scans in a volunteer in which separate acquisitions were done with the 12-active-coil and 32-active-coil approaches using the accelerated DCE-MRI sequence without contrast injection. Unaccelerated coil calibration image sets were also acquired with both approaches. Data from the 32-coil acquisition were reconstructed two ways: (i) using all 32 coils; and (ii) using data from only the same 12 coils as for the 12-active-coil acquisition. Reconstruction (iii) was done using all 12 coils of the 12-active-coil acquisition.

The images from reconstructions (i), (ii), and (iii) were compared in two ways. First, images of absolute SNR were formed from data sets (i), (ii), and (iii) using the method of Refs [25,26]. As the coil sensitivity profiles used in these calculations were estimated empirically via the root-sum-of-square demodulation, these SNR values are quantitatively approximate. Reconstructed SNR values were taken of a 3D volume just encompassing the prostate, in this case approximately 65 cm<sup>3</sup> and comprised of >20,000 pixels. Second, using the coil calibration data and assuming the acceleration factors of the DCE-MRI sequence in Table 2, images were formed of the g-factor, a mathematical measure of the ability of a receiver coil array to retain SNR in accelerated MR acquisition [23]. These comparisons, shown in Fig. 2, indicated that the SNR (A) and g-factor statistics (B) of reconstructions (ii) and (iii) were essentially indistinguishable, and both were different from results for reconstruction (i). Consequently, results for the 12-coil reconstruction were generated in the patient study by selecting data only from those 12

elements from the 32-active-coil acquisition and reconstructing that data. Comparisons were then made with the reconstruction using the full 32-coil data set.

#### 2.5. Radiological evaluation

For each of the 50 patient studies the 32-coil DCE-MRI sequence was reconstructed, and images were zero padded by a factor of 2 and cropped to effectively magnify the region surrounding the prostate. An observer not performing the radiological evaluation selected an axial partition midway through the S/I extent of the prostate at the time frame closest to 50 s post injection. This typically corresponded to a time 10 to 20 s after peak contrast enhancement of any rapidly enhancing lesions in the prostate. The magnified 32-coil and 12-coil images from this partition and time frame were then placed side-by-side randomly and in blinded fashion for each study. This set of 50 composite images was then provided to each reviewer.

The two radiologist reviewers (ATF, six years' experience in prostate MRI; AK, 20 years' experience) then independently graded each image pair using a five-point scale (−2 = left (L) image significantly better than right (R) image; −1 = L slightly better than R; 0 = L and R images equivalent; +1 = R slightly better than L; +2 = R significantly better than L). This was done for each of the four criteria of perceived SNR, level of artifact, sharpness, and overall preference.

In addition, images of absolute SNR were made for the 32-coil and 12-coil reconstructions for each of the studies using the coil calibration images as described previously for the volunteer study. For this analysis images from the six of the 50 patients who were imaged post-prostatectomy were excluded. For each study the 3D rectangular volume was identified on the reconstructed images which just encompassed the prostate, histograms of the SNR values were generated for all voxels within the volume for the two reconstructions, and the ratio of median values of the 32-coil vs. 12-coil histograms was taken as a measure of SNR improvement for that study. These volumes ranged from 28 to 265 cm<sup>3</sup> with a median of 101 cm<sup>3</sup>, typically including several tens of thousands of pixels. This process was repeated for the g-factor for the acceleration used in the DCE-MRI run, and the ratio of median g-factor values determined.

#### 2.6. Statistical significance

For the radiological evaluation after accounting for the blinded presentation, significant (defined as  $p < 0.05$ ) difference from the null hypothesis of equivalent performance was assessed with the Wilcoxon signed rank test.

#### 2.7. Extension to other pulse sequences for prostate MRI

After having demonstrated improved performance in prostate DCE-MRI, it was of interest to assess potential improvement in the other sequences of multi-parametric prostate MRI, namely T2-weighted spin-echo (T2SE) and diffusion-weighted imaging (DWI). This was not possible with the 50 patient studies described previously. To study this in a controlled manner a phantom was used, consisting of a plastic, male-like pelvic shell filled with B-gel, sorbic acid, and salt dissolved in water which upon congealing mimics soft tissue. During the pouring two inclusions were added, one a 50 cm<sup>3</sup> balloon to mimic the bladder and the second a 40 cm<sup>3</sup> balloon to mimic the prostate. For both balloons the B-gel concentration was adjusted to provide slight but discernible signal differences vs. background. A photograph of the phantom is shown in Fig. 8A. Based on phantom size, it corresponds to a BMI of approximately 24.

The phantom was imaged with the 12- and 32-coil arrangements using the sequences: (i) DCE-MRI described above, (ii) coronal T2SE, (iii) full lateral-FOV "conventional" axial DWI, and (iv) limited-lateral-FOV axial DWI [27]. Sequence parameters are shown in Table 3. The

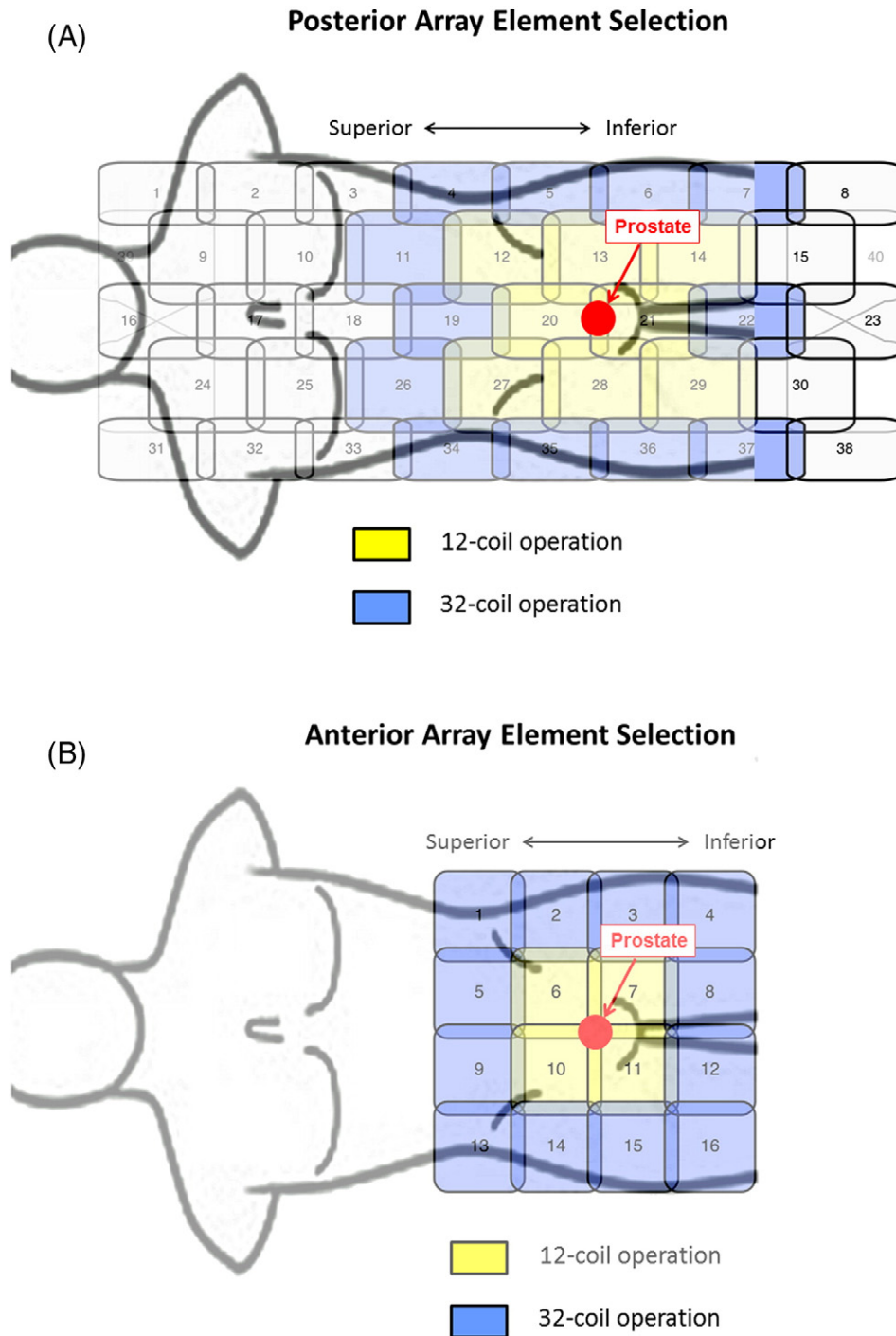


**Fig. 1.** Schematics of coil elements and element selection for 12-coil and 32-coil operation. (A) 40-element GEM array contained within the patient table and located posterior to the supine patient. (B) Schematic of 16-element array placed anteriorly to the supine patient. For 12-channel operation the coil elements shown in yellow are selected, eight from the posterior array and four from the anterior array. For 32-channel operation all coils in yellow and additionally those in blue are selected. For the posterior GEM array signals from the lateral-most elements are paired (4 with 34, 5 with 35, etc.) and combined in hardware into one virtual coil per pair. For 32-channel operation all 16 elements of the anterior array are used.

DCE-MRI data was used to reconstruct 3D images of absolute SNR as described previously, and the ratio between the 32- vs. 12-coil images taken as a measure of absolute intrinsic SNR improvement. Each of the other sequences was run twice, the same gain settings for both runs. For each sequence an image from one of the runs was selected of a section midway through the prostate inclusion. The signal  $S$  was taken as the mean over a circular, approximate  $2 \text{ cm}^2$  region-of-interest (ROI) within the inclusion. Noise  $\sigma$  was assessed by forming the difference image between the two acquired images of the same anatomic section,

measuring the standard deviation in the same ROI as used for signal, and dividing the result by  $\sqrt{2}$  to account for the subtraction. SNR was then defined as  $S/\sigma$ , and the ratio of SNRs of 32- and 12-coil acquisition determined.

### 3. Results

Fig. 2B shows the cumulative histograms of the g-factor values for the 32-coil and 12-coil reconstructions. The solid green, blue, and red

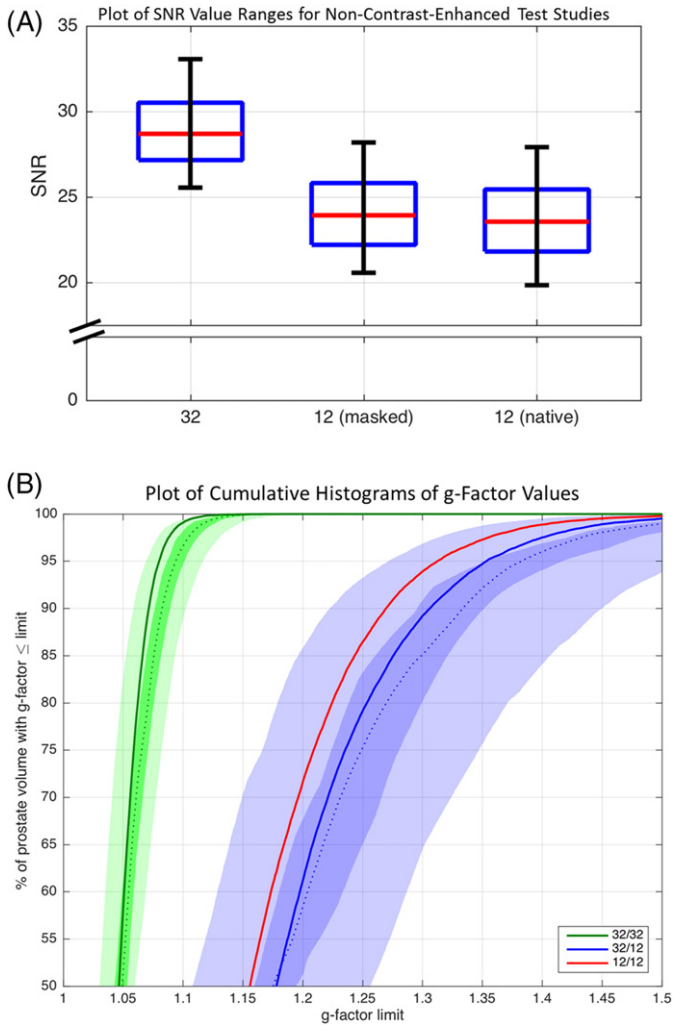


**Fig. 2.** (A) Box and whisker plots of the reconstructed SNR values from the non-contrast-enhanced test case evaluating reconstructions (i) 32-coil acquisition with 32-coil reconstruction, (ii) 32-coil acquisition with 12-coil reconstruction (“masked”), and (iii) 12-coil acquisition with 12-coil reconstruction (“native”). Each figure shows the median, ±25% values (box boundaries), and ±45% boundaries (whiskers). Median values are 28.7, 23.9, and 23.5 (a.u.). (B) Plot of the cumulative g-factor statistics for the 32-channel acquisition with 32-coil (green lines and curves) and 12-coil (blue lines and curves) reconstructions and for the 12-channel acquisition with 12-coil reconstruction (solid red line). The three solid curves are for the non-contrast-enhanced test scans. The shaded green and blue zones show the ranges of g-factor values measured across the 32-coil and 12-coil reconstructions for all 50 patient studies, respectively. The dotted green and blue lines correspond to the median values, the dark shaded zones to ±12.5% about the median and the light shaded zones to ±37.5% about the median. For all plots the statistics are measured over the 3D volume encompassing the prostate.

lines are for the unenhanced test scans of the volunteer. The green shaded region shows the cumulative g-factor histogram for the 32-coil reconstruction based upon all 50 patient studies. The dashed green line is the median value; the dark green zone encompasses the central 25%, and the light green zone the central 75% at that cumulative percentage. Similarly, the blue shaded region shows analogous results for the 12-coil reconstruction. The more rapid approach to 100% of the green 32-coil reconstruction indicates the overall smaller g-factor values and better retention of SNR vs. the two 12-coil reconstructions (blue curves and blue regions and red curve). This distinction between curves is maintained across all 50 patient studies in that the shaded green and blue regions are well separated. The close match of the blue regions and red curve indicates the equivalence in performance of reconstruction (ii) and (iii).

Fig. 3 shows results from the qualitative evaluation of the two radiologists. 32-coil reconstruction (positive scores) was evaluated as

**Table 3**

Technical parameters of T2SE and DWI pulse sequences used for phantom-based SNR analysis.

Parameter	T2SE	Conventional DWI	Limited-FOV DWI
Format	Coronal	Axial	Axial
Field of View (mm <sup>2</sup> ) (FOV <sub>x</sub> × FOV <sub>y</sub> )	220 × 220	360 × 360	260 × 130
Acquisition matrix (X × Y)	320 × 320	192 × 192	144 × 72
Inplane resolution (mm <sup>2</sup> ) (X × Y)	0.688 × 0.688	1.875 × 1.875	1.8 × 1.8
Slice Thickness/spacing (mm for both)	3/3.3	3/0	4/0
TR (ms)	4951	5888	3925
TE (ms)	96	70	75
Number of slices	26	23	16
b-Values (s/mm <sup>2</sup> )	–	100/1000	100/1000
Number of averages	1	1	1

The T2SE sequence used a fast-spin-echo readout with an echo train length of 4.

significantly superior ( $p < 0.001$ ) to 12-coil reconstruction using the criteria of SNR (A) and overall preference (D) by both reviewers individually and in aggregate. 32-coil and 12-coil reconstructions were evaluated as equivalent for the criteria of level of artifact (B) and sharpness (C) by both reviewers individually and in aggregate. For perceived SNR the two reviewers' scores matched in 38/50 cases and were within one value on the five-point –2 to +2 scale in all 50/50. For artifact these corresponding results were 34/50 and 50/50; for sharpness 27/50 and 46/50; for overall preference 22/50 and 47/50.

Fig. 4 shows the percent improvement in SNR values provided by the 32-coil vs. 12-coil reconstruction plotted vs. the BMI of the patient. The red circles show the case with no acceleration, as determined from the images of SNR using the coil calibration data. The median increase (18%) over the 44 studies is noted with the red hashmark on the ordinate axis, and the trend line, determined by least squares regression,

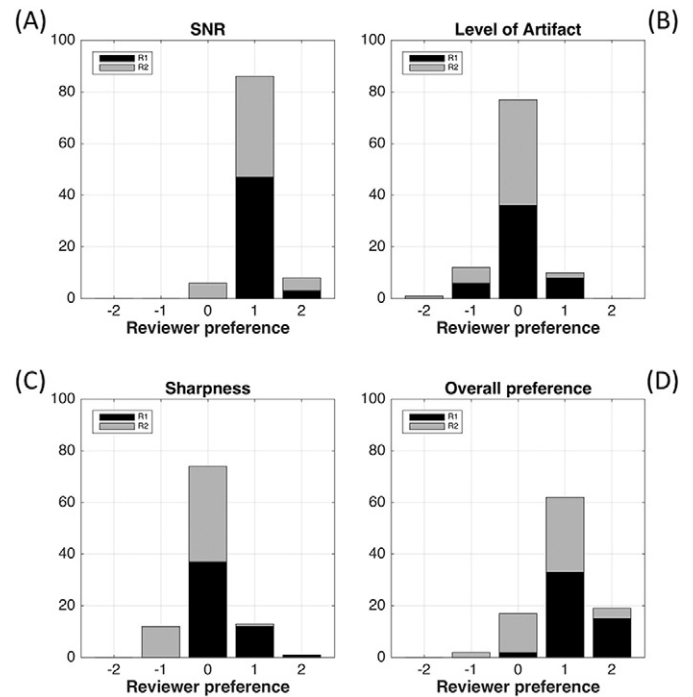


**Fig. 3.** Histograms showing the results of the radiological review for perceived SNR (A), level of artifact (B), sharpness (C), and overall preference (D). For SNR (A) and overall preference (D) the preference for the 32-coil reconstruction (positive scores) was significant ( $p < 0.001$ ) for both reviewers individually and in aggregate. For artifact (B) and sharpness (C) there was no significant preference.

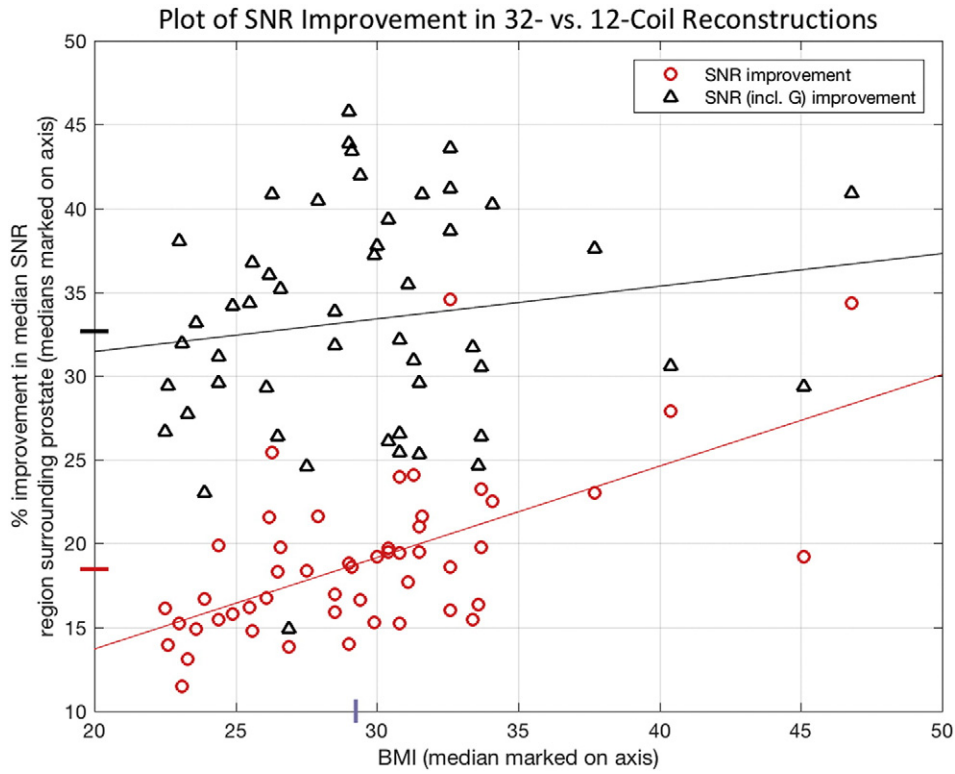


**Fig. 4.** Plot of the ratio of median reconstructed SNR values without (red circles) and with (black triangles) the additional effect of g-factor improvements for the 32-coil and 12-coil reconstructions plotted vs. BMI of the patient. In each case values were computed from a volume encompassing the prostate. The median increase for each is shown in the corresponding colored hashmark on the ordinate, and trend lines of each with BMI, as determined from least square regression, are also noted.

shown in red. The triangles show the case when acceleration is additionally used at the acceleration factors employed in this study with analogous median (32%) and trend lines shown in black. The median BMI (29.1) for the 50 studies is also noted as a hashmark on the abscissa.

Figs. 5-7 show sample results from three patient studies in which the 32-coil and 12-coil reconstructions are compared. Video V1 compares all 31 time frames for 12- vs. 32-coil reconstructions for the study presented in Fig. 5.

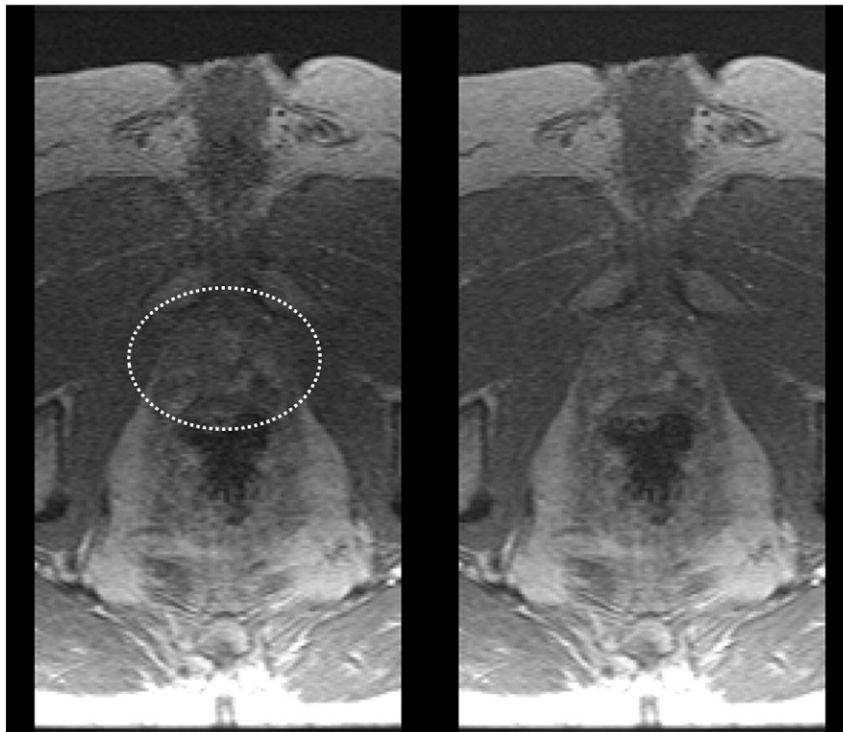


**Fig. 5.** Comparison of 12-coil (left) and 32-coil (right) reconstructions of prostate DCE-MRI in a patient with BMI 26.6. Prostate is identified within the white ellipse. Radiologists #1 and #2 both assigned scores of (+2, 0, 0, +2) for (perceived SNR, artifact level, sharpness, overall preference) where positive scores reflect preference for the 32-coil result.

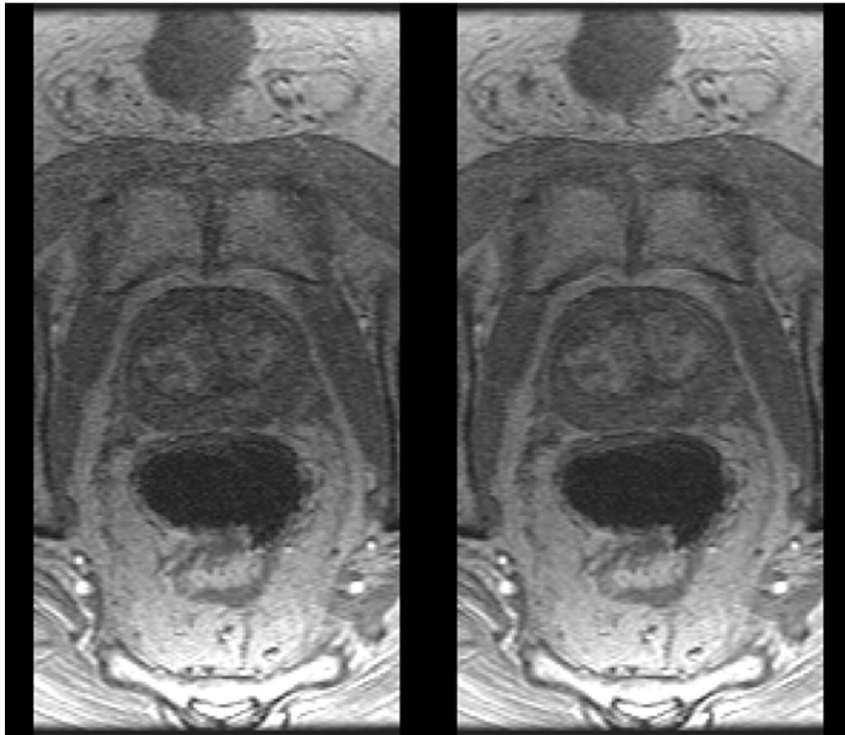


**Fig. 6.** Comparison of 12-coil (left) and 32-coil (right) reconstructions of prostate DCE-MRI in a patient with BMI 30.4. Radiologists #1 and #2 assigned scores of (+1, 0, 0, +1) and (+1, 0, 0, +2).

Table 4 summarizes results for relative SNR for the phantom studies which show an SNR increase ranging from 9.7% for T2SE to 34.3% for the b-1000 conventional DWI. Fig. 8B is a axial image of the phantom showing the SNR increase determined from the DCE-MRI coil calibration data.

The position of the prostate inclusion is designated by the dashed circle. Fig. 8C is a side-by-side comparison of unsubtracted coronal T2SE images of the phantom using 12- (left) and 32-coil (right) acquisition illustrating the size and placement of the bladder and prostate inclusions.

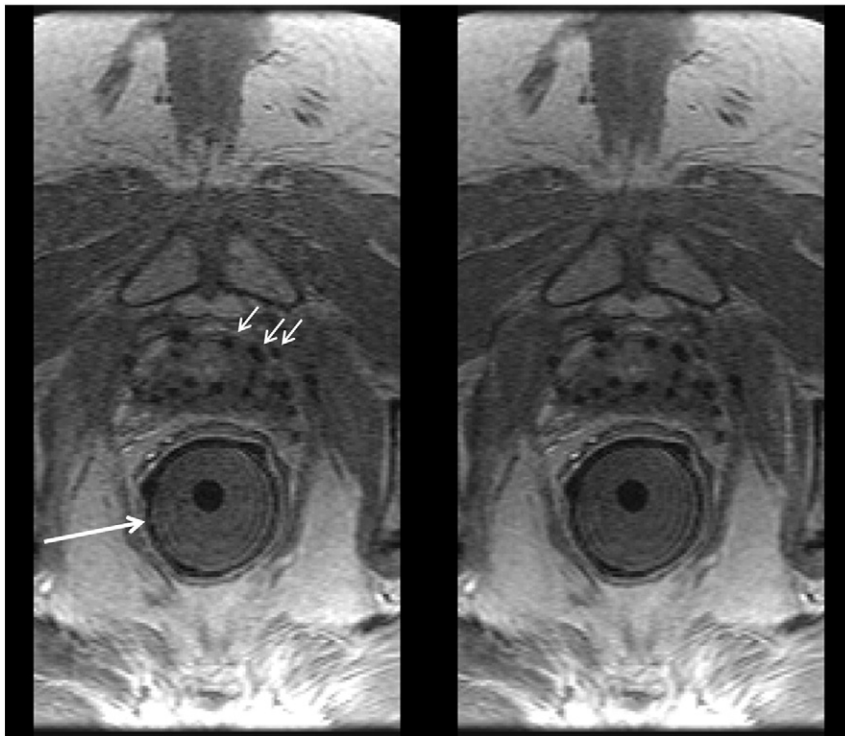


**Fig. 7.** Comparison of 12-coil (left) and 32-coil (right) reconstructions of prostate DCE-MRI in a patient with BMI 33.4 and with implanted seeds for brachytherapy (black dropouts, e.g. short white arrows). In this exam an endorectal coil used for sequences other than DCE-MRI was applied within a gel-filled insert (long white arrow) but not active for the DCE-MRI sequence. Radiologists #1 and #2 assigned scores of (+1, 0, 0, +1) and (0, 0, 0, 0).

**Table 4**  
Relative SNR of 32- vs. 12-coil acquisition as measured in prostate phantom.

Comparison	Sequence	Relative SNR
1	T2SE	1.097
2	Conventional DWI ( $b = 100 \text{ s/mm}^2$ , 1 average)	1.163
3	Conventional DWI ( $b = 1000 \text{ s/mm}^2$ , 1 average)	1.346
4	Limited-FOV DWI ( $b = 100 \text{ s/mm}^2$ , 1 average)	1.116
5	Limited-FOV DWI ( $b = 1000 \text{ s/mm}^2$ , 1 average)	1.338

#### 4. Discussion

For the same level of acceleration, the acquisition and reconstruction of data from 32 receiver coils encompassing the pelvis provides superior measured and perceived SNR in dynamic-contrast-enhanced prostate MRI vs. use of the vendor-recommended 12 receiver coils. The median improvement in overall measured SNR was 32% over the volume of the prostate. Although the placement of the 12 receiver elements used already encompasses the full lateral and superior/inferior extent of the prostate, the incorporation of data from additional coils can provide improved performance without generation of artifact related to the increase in number of elements.

There are possible disadvantages in the use of additional receiver coils in image reconstruction. When done on the vendor system, the reconstruction time for a 32-coil DCE-MRI run is 50 s vs. 15 s on our custom hardware. Lacking high speed computational hardware, reconstruction time can possibly be reduced by grouping coil elements together before digitization to reduce the overall number of data channels [28,29]. However, as commercial systems continue to improve in the future, reconstruction times are expected to decrease and make this less of an issue.

Another possible disadvantage in the use of incremental coils located somewhat distantly from the FOV of interest is that motion of distant objects might alias into the reconstructed FOV owing to the high sensitivity of the incremental coils to the moving object. The evaluation performed in this work indicated that this was not a significant problem. If artifact were present and could be associated with some specific distant body region, then conceivably the reconstruction could be repeated with data from the coils nearby to that region excluded.

In this work data from each 32-coil DCE-MRI acquisition were reconstructed two ways, the first using all 32 coils and the second using only 12 coils, and the results compared. This study design eliminated the additional uncertainty and expense associated with a study in which each subject would have been imaged twice with contrast material, once with each coil set. We validated this approach by comparing 12-coil reconstruction from 32- and 12-coil acquisitions and showed negligible difference in SNR and g-factor.

This study evaluated two vendor-provided configurations of the coil arrays available with the MRI system. It is possible that other configurations might provide improved performance. Specifically, acceleration applied along a particular direction benefits from coil elements which tend to face each other along that direction. Electrically combining the two most lateral elements of the GEM array into one virtual coil, as done by the vendor, might not be optimal for this array for L/R acceleration. Also, other styles of receiver coil arrays may provide improved performance, such as arrays placed in better proximity or wrapped around the pelvis. Incorporation of an endorectal coil can be expected to provide some improvement in SNR near that coil. In this work although an endorectal coil was placed in some subjects as seen in Fig. 7, it was active only for sequences other than DCE-MRI.

The quantitative analysis distinguished between SNR improvement solely due to the increase in the number of coils in an unaccelerated scan (red dots of Fig. 4) as well as that due to improvement in g-factor

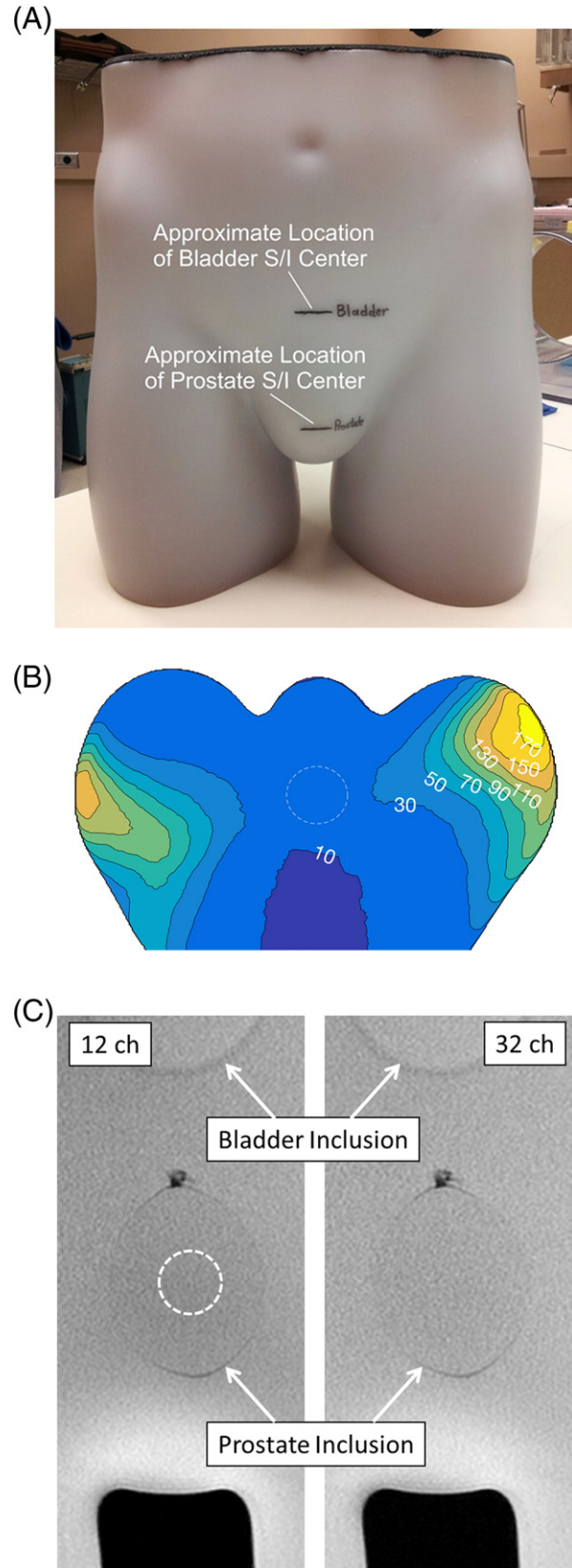


**Fig. 8.** (A) Photograph of phantom used for assessment of prostate MRI. Superior/inferior levels of bladder and prostate inclusions are noted. (B) Axial image of the phantom at the level of prostate inclusion (dashed circle) showing relative percent improvement in SNR of 32- vs. 12-coil acquisition. (C) Coronal T2SE images of the phantom acquired using 12- (left) and 32-coil (right) acquisitions. The observed 9.7% SNR increase is difficult to visualize, but the images show the size and location of the prostate inclusion. ROI used for SNR measurement is indicated as dashed ellipse (left image).

statistics (increment between red dot and black triangle for each patient) at the specific acceleration factor used. The first of these should benefit any sequence. The 32-coil array provided improvement in both SNR and in g-factor statistics vs. the 12-coil array. Both are important in acquisitions such as DCE-MRI in which acceleration is used. It is interesting that the level of improvement of SNR (red circles of Fig. 4) appeared to correlate positively with BMI.

Extending this to sequences beyond DCE-MRI, the phantom study results in Table 4 indicate that both T2SE and DWI are expected to benefit with improved SNR with 32-coil acquisition. Consistent with the results shown, sequences which are particularly signal-starved, such as high-b value DWI, might in practice benefit more from the SNR increase. This can potentially be used to reduce the level of averaging commonly done in DWI.

The benefit of increased SNR can be used for DCE-MRI in various ways. As stated, we initially investigated but opted not to go to faster frame rates. We have developed a version for assessment of biochemical recurrence with higher spatial resolution ( $0.76 \times 0.87 \times 2.24 \text{ mm}^3$  vs. the  $0.86 \times 1.15 \times 3.0 \text{ mm}^3$  of this work) with a 15 s vs. 6.6 s frame time.

In addition to the above-described extended reconstruction time and possible motion artifact from distant objects, another limitation of this work is that further study is necessary to determine whether prostate lesion detection and characterization are improved with 32-coil DCE-MRI. Also, study of the impact in T2SE and DWI sequences should be extended to a detailed patient series for a more complete assessment.

In summary, for the same level of acceleration, the acquisition and reconstruction of data from 32 receiver coils encompassing the pelvis provides superior measured and perceived SNR in dynamic-contrast-enhanced prostate MRI vs. use of 12 receiver coils.

Supplementary data to this article can be found online at <http://dx.doi.org/10.1016/j.mri.2017.01.017>.

## Funding

NIH EB000212, EB017840, RR018898; DOD W81XWH-15-1-0341; NSF CIF:1818347.

## Acknowledgments

We acknowledge the assistance of Brent A. Warndahl in performing the studies.

## References

- [1] Delongchamps NB, Rouanne M, Flam T, et al. Multiparametric magnetic resonance imaging for the detection and localization of prostate cancer: combination of T2-weighted, dynamic contrast-enhanced and diffusion-weighted imaging. *BJU Int* 2010;107:1411–8.
- [2] Dickinson L, Ahmed HU, Allen C, et al. Magnetic resonance imaging for the detection, localization, and characterization of prostate cancer: recommendations from a European consensus meeting. *Eur Urol* 2011;59:477–94.
- [3] Barentz JO, Richenberg J, Clements R, et al. ESUR prostate MR guidelines 2012. *Eur Radiol* 2012;22:746–57.
- [4] Franiet T, Hamm B, Hricak H. Dynamic contrast-enhanced magnetic resonance imaging and pharmacokinetic models in prostate cancer. *Eur Radiol* 2011;21:616–26.
- [5] Verma S, Turkbey B, Muradyan N, et al. Overview of dynamic contrast-enhanced MRI in prostate cancer diagnosis and management. *AJR* 2012;198:1277–88.
- [6] Rosenkrantz AB, Geppert C, Grimm R, et al. Dynamic contrast-enhanced MRI of the prostate with high spatiotemporal resolution using compressed sensing, parallel imaging, and continuous golden-angle radial sampling: preliminary experience. *J Magn Reson Imaging* 2015;41:1365–73.
- [7] Weinreb JC, Barentz JO, Choyke PL, et al. PI-RADS prostate imaging - reporting and data system: 2015, version 2. *Eur Urol* 2016;69:16–40.
- [8] Han M, Partin AW, Zahurak M, Piantadosi S, Epstein JI, Walsh PC. Biochemical (prostate specific antigen) recurrence probability following radical prostatectomy for clinically localized prostate cancer. *J Urol* 2003;169:517–23.
- [9] Trock BJ, Han M, Freedland SJ, et al. Prostate cancer-specific survival following salvage radiotherapy vs. observation in men with biochemical recurrence after radical prostatectomy. *JAMA* 2010;299:2760–9.
- [10] Rouviere O, Vitry T, Lyonnet D. Imaging of prostate cancer local recurrences: why and how? *Eur Radiol* 2010;20:1254–66.
- [11] Kitajima K, Hartmann RP, Froemming AT, Hagen CE, Takahashi N, Kawashima A. Detection of local recurrence of prostate cancer after radical prostatectomy using endorectal coil MRI at 3 T: addition of DWI and dynamic contrast enhancement to T2-weighted MRI. *AJR* 2015;205:807–16.
- [12] Attenberger UI, Ingrisch M, Dietrich O, et al. Time-resolved 3D pulmonary perfusion MRI: comparison of different k-space acquisition strategies at 1.5 and 3 T. *Invest Radiol* 2009;44:525–31.
- [13] Park BK, Kim B, Kim CK, Lee HM, Kwon GY. Comparison of phased-array 3.0-T and endorectal 1.5-T magnetic resonance imaging in the evaluation of local staging accuracy for prostate cancer. *J Comput Assist Tomogr* 2007;31(4):534–8.
- [14] Heijmink SW, Futterer JJ, Hambroek T, et al. Prostate cancer; body-array versus endorectal coil MR imaging at 3 T - comparison of image quality, localization, and staging performance. *Radiology* 2007;244(1):184–95.
- [15] Mazaheri Y, Vargas HA, Nyman G, Shukla-Dave A, Akin O, Hricak H. Diffusion-weighted MRI of the prostate at 3.0 T: comparison of endorectal coil (ERC) and phased-array coil (PAC) MRI - the impact of SNR on ADC measurement. *Eur J Radiol* 2013;82:e515–20.
- [16] Turkbey B, Merino MJ, Gallardo EC, et al. Comparison of endorectal coil and nonendorectal coil T2 W and diffusion-weighted MRI at 3 Tesla for localizing prostate cancer: correlation with whole-mount histopathology. *J Magn Reson* 2014;39:1443–8.
- [17] Hotker AM, Mazaheri Y, Aras O, et al. Assessment of prostate cancer aggressiveness by use of the combination of quantitative DWI and dynamic contrast-enhanced MRI. *AJR* 2016;206:756–63.
- [18] Ocak I, Bernardo M, Metzger G, et al. Dynamic contrast-enhanced MRI of prostate cancer at 3 T: a study of pharmacokinetic parameters. *AJR* 2007;189:W192–201.
- [19] Fennessy FM, Fedorov A, Penzkofer T, et al. Quantitative pharmacokinetic analysis of prostate cancer DCE-MRI at 3 T: comparison of two arterial input functions on cancer detection with digitized whole mount histopathological validation. *Magn Reson* 2015;33:886–94.
- [20] Cho E, Chung DJ, Yeo DM, et al. Optimal cut-off value of perfusion parameters for diagnosing prostate cancer and for assessing aggressiveness associated with Gleason score. *Clinical Img* 2015;39:834–40.
- [21] Haider CR, Hu HH, Campeau NG, Huston III J, Riederer SJ. 3D high temporal and spatial resolution contrast-enhanced MR angiography of the whole brain. *Magn Reson Med* 2008;60:749–60.
- [22] Riederer SJ, Tasciyan T, Farzaneh F, Lee JN, Wright RC, Herfkens RJ. MR fluoroscopy: technical feasibility. *Magn Reson Med* 1988;8:1–15.
- [23] Pruessmann KP, Weiger M, Scheidegger MB, Boesiger P. SENSE: sensitivity encoding for fast MRI. *Magn Reson Med* 1999;42:952–62.
- [24] Borisch EA, Trzasko JD, Froemming AT, et al. Faster-than-acquisition 4D sparse reconstruction for Cartesian 2D SENSE-type acquisition. 23rd Annual Mtg. Toronto: ISMRM; 2015. p. 1580.
- [25] Kellman P, McVeigh ER. Image reconstruction in SNR units: a general method for SNR measurement. *Magn Reson Med* 2005;54:1439–47.
- [26] Kellman P, McVeigh ER. Erratum to Kellman P, McVeigh ER. Image reconstruction in SNR units: a general method for SNR measurement. *Magn Reson Med* 2005;54:1439–1447. *Magn Reson Med* 2007;58:211–2.
- [27] Feng Z, Min X, Kumar Sah V, et al. Comparison of field-of-view (FOV) optimized and constrained undistorted single shot (FOCUS) with conventional DWI for the evaluation of prostate cancer. *Clinical Img* 2015;39:851–5.
- [28] Buehrer M, Pruessmann KP, Boesiger P, Kozerke S. Array compression for MRI with large coil arrays. *Magn Reson Med* 2007;57:1131–9.
- [29] Beatty PJ, Chang S, Holmes JH, et al. Design of k-space channel combination kernels and integration with parallel imaging. *Magn Reson Med* 2014;71:2139–54.



Original contribution

## Robust and efficient pharmacokinetic parameter non-linear least squares estimation for dynamic contrast enhanced MRI of the prostate

Soudabeh Kargar<sup>a,b</sup>, Eric A. Borisch<sup>b</sup>, Adam T. Froemming<sup>b</sup>, Akira Kawashima<sup>c</sup>, Lance A. Mynderse<sup>d</sup>, Eric G. Stinson<sup>b</sup>, Joshua D. Trzasko<sup>b</sup>, Stephen J. Riederer<sup>a,b,\*</sup>

<sup>a</sup> Biomedical Engineering and Physiology Program, Mayo Graduate School, Rochester, MN, United States

<sup>b</sup> Department of Radiology, Mayo Clinic, Rochester, MN, United States

<sup>c</sup> Department of Radiology, Mayo Clinic, Scottsdale, AZ, United States

<sup>d</sup> Department of Urology, Mayo Clinic, Rochester, MN, United States



### ARTICLE INFO

#### Keywords:

Prostate cancer  
Dynamic-contrast-enhanced magnetic resonance imaging  
Pharmacokinetic modeling  
Perfusion  
Multi-parametric magnetic resonance imaging

### ABSTRACT

**Purpose:** To describe an efficient numerical optimization technique using non-linear least squares to estimate perfusion parameters for the Tofts and extended Tofts models from dynamic contrast enhanced (DCE) MRI data and apply the technique to prostate cancer.

**Methods:** Parameters were estimated by fitting the two Tofts-based perfusion models to the acquired data via non-linear least squares. We apply Variable Projection (VP) to convert the fitting problem from a multi-dimensional to a one-dimensional line search to improve computational efficiency and robustness. Using simulation and DCE-MRI studies in twenty patients with suspected prostate cancer, the VP-based solver was compared against the traditional Levenberg-Marquardt (LM) strategy for accuracy, noise amplification, robustness to converge, and computation time.

**Results:** The simulation demonstrated that VP and LM were both accurate in that the medians closely matched assumed values across typical signal to noise ratio (SNR) levels for both Tofts models. VP and LM showed similar noise sensitivity. Studies using the patient data showed that the VP method reliably converged and matched results from LM with approximate  $3 \times$  and  $2 \times$  reductions in computation time for the standard (two-parameter) and extended (three-parameter) Tofts models. While LM failed to converge in 14% of the patient data, VP converged in the ideal 100%.

**Conclusion:** The VP-based method for non-linear least squares estimation of perfusion parameters for prostate MRI is equivalent in accuracy and robustness to noise, while being more reliably (100%) convergent and computationally about  $3 \times$  (TM) and  $2 \times$  (ETM) faster than the LM-based method.

### 1. Introduction

Perfusion imaging via dynamic contrast-enhanced (DCE) MRI uses pathological angiogenesis as a biomarker for differentiation of cancerous vs. normal tissue [1]. In tumors, due to abnormal angiogenesis, there is a corresponding increase in the amount of blood delivered to the capillary bed and perfusing the tissue, and this can be detectable with MRI. A number of perfusion models applicable to DCE-MRI have been proposed [2–4]. Among these models, the Tofts model (TM) [5] and extended Tofts model (ETM) [6] are often used in perfusion analysis [7–23]. In the two-parameter TM, the perfusion parameters  $K^{trans}$ , the volume transfer constant between blood plasma and extra-vascular extra-cellular space (EES), and  $k_{ep}$ , the rate constant, are estimated from the DCE-MRI data.  $K^{trans}$  and  $k_{ep}$  are related by  $k_{ep} = K^{trans}/v_e$ , where  $v_e$

represents the fractional volume of the EES. With the ETM, a third parameter, the vascular fractional volume,  $v_p$ , is also allowed. It is known that parameters  $K^{trans}$  and  $k_{ep}$  both tend to increase in malignant vs. benign tissue [24–28]. Thus, it is desirable to obtain accurate estimates of these parameters.

The contrast concentration vs. time curves from DCE-MRI are used to estimate the pharmacokinetic parameters by fitting a perfusion model to the acquired data. This is done traditionally by using an implementation of non-linear or linear least-squares estimation [29]. Non-linear least squares (NLLS) such as the Levenberg-Marquardt (LM) algorithm [30,31] allow mathematical flexibility in the perfusion model but often require an iterative search and selecting the initial search point. NLLS methods have been used in DCE-MRI [32–34]. Use of multiple search starting points can provide higher accuracy in the

\* Corresponding author at: Biomedical Engineering and Physiology Program, Mayo Graduate School, Rochester, MN, United States.  
E-mail address: [riederer@mayo.edu](mailto:riederer@mayo.edu) (S.J. Riederer).

results but with increased computation time [33]. Linear least squares (LLSQ) optimizations have also been used in DCE-MRI [32,34,35]. However, the linearization of a non-linear problem can result in differences in data weighting and possible bias [34,36].

The goal of this work is to use the variable projection (VP) approach [37] to develop a robust and efficient numerical optimization strategy which addresses current limitations of both NLLS and LLSQ methods in DCE-MRI. The VP-based NLLS framework arises naturally from the TM and ETM perfusion models with no additional assumptions or simplifications. At the same time, the VP-based approach is shown to have superior characteristics such as speed, simplicity of implementation, and overall robustness vs. a widely-used NLLS implementation, LM.

The fitting algorithm presented here is based on the general approach of variable projection (VARPRO or “VP”), described in the mathematical literature several decades ago [37]. This approach reduces the dimensionality of the problem of estimation of multiple parameters from a data set according to some mathematical model and has been used in multiple applications. Examples in MR include determining the localized polynomial approximation parameters for model-based reconstruction [38], MR spectroscopy [39–41],  $T_1$  mapping in single [42] and multichannel [43] acquisition,  $T_{1\rho}$  mapping as a biomarker for liver cirrhosis [44], fat-water estimation [45–50], and MR fingerprinting [51]. Variable projection has been also used in kinetic parameter estimation of DCE-MRI to account for an unknown arterial input function (AIF) via multichannel blind identification [52,53]. However, to our knowledge VARPRO has not been applied to the TM and ETM where the perfusion parameters are estimated with this technique.

The VP-based method for estimating the perfusion parameters is presented here in the context of prostate cancer, the most common non-cutaneous cancer among men in the United States [54]. If found in its early stages, a number of treatment options can lead to high survival rates. Due to the limited specificity of monitoring the prostate specific antigen (PSA) level the use of MRI for diagnosis or staging of prostate cancer has increased in recent years. Prostate MRI is typically performed using a multi-parametric MRI (mpMRI) exam [55–57] which includes  $T_2$ -weighted spin-echo (T2SE), diffusion-weighted imaging (DWI), and  $T_1$ -weighted DCE-MRI sequences. Quantitative perfusion based on the DCE-MRI has been widely studied in the prostate [9,18–20,24,27,58–61], and DCE-MRI plays a role in risk stratification for patients with suspected prostate cancer in the PI-RADS v2 reporting system [57]. DCE-MRI is especially important in the evaluation of local recurrence after radiotherapy or radical prostatectomy [62,63].

In the following sections we derive formulas for DCE-MRI perfusion parameter estimation for the TM and ETM using the VARPRO approach, compare performance with traditional Levenberg-Marquardt methods, and demonstrate its applicability in a group of 20 patients with known prostate cancer as validated by histology. This work is an expansion of material presented previously in abstract form [64,65].

## 2. Materials and methods

### 2.1. Parameter estimation using VARPRO for the Tofts model

Perfusion is modeled as a two compartment system in which a low-molecular weight gadolinium contrast agent can diffuse out of the blood vessels into the EES but not enter the cells. Therefore, the two compartments of the tracer distribution are the blood plasma and the EES. In the derivations which follow, lower and upper case bold denote vector and matrix, respectively,  $[\cdot]^*$  denotes the conjugate transpose of  $[\cdot]$ , and  $[\cdot]_t$  denotes that the first dimension of  $[\cdot]$  has length  $N$ , with each entry corresponding to a different time  $t$  for  $N$  total time frames. Using the original Tofts model (TM) [5] the modeled tissue contrast concentration  $p(t)$  is given by Eq. (1) for each voxel:

$$p(t) = K^{trans} \int_0^t a(\tau) e^{-k_{ep}(t-\tau)} d\tau \quad (1)$$

where  $K^{trans}$  and  $k_{ep}$  are the transfer constant and rate constant respectively, each measured in  $\text{min}^{-1}$ , and  $a(\tau)$  is the measured or assumed AIF. This integral form of the TM can subsequently be discretized to yield:

$$\mathbf{p}_t = \mathbf{a}_t \otimes \mathbf{h}_t(k_{ep}) K^{trans} \quad (2)$$

where  $\otimes$  is the convolution operator and  $\mathbf{a}_t$  and  $\mathbf{p}_t$  are the vector versions of  $a(t)$  and  $p(t)$ . Also note that  $\mathbf{h}_t(k_{ep})$  is defined as  $e^{-k_{ep}t}$ . Eq. (2) can be re-expressed in linear algebraic form using the  $N \times N$  matrix  $\mathbf{A}$  comprised of elements of  $\mathbf{a}_t$ :

$$\mathbf{p}_t = \mathbf{A} \mathbf{h}_t(k_{ep}) K^{trans} \quad (3)$$

where  $\mathbf{A}$  is given by:

$$\mathbf{A} = \begin{bmatrix} a_0 & 0 & 0 & 0 \\ a_1 & a_0 & 0 & 0 \\ a_2 & a_1 & a_0 & 0 \\ \vdots & \vdots & \vdots & \\ a_N & a_{N-1} & \dots & a_0 \end{bmatrix} \quad (4)$$

and zero-padded boundary conditions are assumed to include only the first  $N$  points to match the acquired perfusion data,  $\mathbf{c}_t$ .

The goal of pharmacokinetic parameter estimation is to fit the model  $\mathbf{p}_t$  to the measurements  $\mathbf{c}_t$  for each voxel of interest. That is to say,  $K^{trans}$  and  $k_{ep}$  are selected to best fit the model,  $\mathbf{p}_t$ , to the measured data,  $\mathbf{c}_t$ .

The discrete parametric model in Eq. (2) can be fit on a pixel-wise basis to the time-course data associated with DCE-MR image series via NLLS regression, wherein the difference between the model as realized with a specific parameter set and the data is minimized. This fitting can be done by first defining the NLLS cost function  $J(K^{trans}, k_{ep})$ :

$$J(K^{trans}, k_{ep}) = \|\mathbf{p}_t - \mathbf{c}_t\|_2^2 = \|\mathbf{A} \mathbf{h}_t(k_{ep}) K^{trans} - \mathbf{c}_t\|_2^2 \quad (5)$$

and minimizing it through some iterative numerical process to find the optimum values of the model parameters,  $\hat{K}^{trans}$  and  $\hat{k}_{ep}$ . For the TM the cost function depends on both  $K^{trans}$  and  $k_{ep}$ , and thus a two-dimensional (2D) optimization problem must be solved for each voxel. As  $J(K^{trans}, k_{ep})$  is quadratic with respect to  $K^{trans}$ , one can derive a closed-form analytical expression for its NLLS-optimal value which will be a (non-linear) function of the other parameter,  $k_{ep}$ , and the data vector,  $\mathbf{c}_t$ . As shown in Appendix A, the closed-form expression for  $\hat{K}^{trans}$  is:

$$\hat{K}^{trans} = \{\mathbf{b}_t^*(k_{ep}) \mathbf{b}_t(k_{ep})\}^{-1} \mathbf{b}_t^*(k_{ep}) \mathbf{c}_t \quad (6)$$

where:

$$\mathbf{b}_t(k_{ep}) = \mathbf{A} \mathbf{h}_t(k_{ep}) \quad (7)$$

Using the VARPRO method, the parametric expression for  $\hat{K}^{trans}$  can then be inserted back into Eq. (5) which causes the dimensionality of  $J$  to be reduced from 2D to 1D. Doing so, as developed further in Appendix A, leads to the following simplified cost function expression:

$$J(\hat{K}^{trans}(k_{ep}), k_{ep}) = -\mathbf{c}_t^* \mathbf{b}_t(k_{ep}) \{\mathbf{b}_t^*(k_{ep}) \mathbf{b}_t(k_{ep})\}^{-1} \mathbf{b}_t^*(k_{ep}) \mathbf{c}_t \quad (8)$$

To find  $\hat{k}_{ep}$  from Eq. (8), one can evaluate the cost function for a range of  $k_{ep}$  values and find the minimum of  $J(\hat{K}^{trans}(k_{ep}), k_{ep})$  via line search. The found  $\hat{k}_{ep}$  is then used to directly determine  $\hat{K}^{trans}$  via Eq. (6), completing the optimization. The simplification in the search for optimum values  $\hat{K}^{trans}$  and  $\hat{k}_{ep}$  provided by VARPRO is illustrated in Supplemental Fig. S1.

### 2.2. Parameter estimation using VARPRO for the extended Tofts model (ETM)

Compared to the standard Tofts Model, the extended Tofts Model

(ETM) has an additional term, the vascular fraction,  $v_p$ , as shown below:

$$p(t) = a(t)v_p + K^{trans} \int_0^t a(\tau)e^{-k_{ep}(t-\tau)}d\tau \quad (9)$$

The VARPRO technique can be applied to the ETM similarly to the TM. Again, the integral form can be expressed in algebraic form but now with the linear terms  $K^{trans}$  and  $v_p$  combined into a vector  $\mathbf{x}$ :

$$\mathbf{p}_t = \mathbf{a}_t v_p + \mathbf{A} \mathbf{h}_t(k_{ep}) K^{trans} = [\mathbf{a}_t \quad \mathbf{A} \mathbf{h}_t(k_{ep})] \begin{bmatrix} v_p \\ K^{trans} \end{bmatrix} = \mathbf{B}_t(k_{ep}) \mathbf{x} \quad (10)$$

where the dimension  $N \times 2$  matrix  $\mathbf{B}_t(k_{ep})$  is defined by:

$$\mathbf{B}_t(k_{ep}) = [\mathbf{a}_t \quad \mathbf{A} \mathbf{h}_t(k_{ep})] \quad (11)$$

Eq. (10) for ETM is similar to Eq. (3) for TM in that the linear term is projected onto the other non-linear term to reduce the dimensionality of the problem to only one dimension. The only difference in ETM is the above-described vector vs. a scalar. The remainder of the optimization of ETM is essentially the same as for the TM, shown in Appendix B, and leading to the results:

$$\hat{\mathbf{x}} = \{\mathbf{B}_t^*(k_{ep}) \mathbf{B}_t(k_{ep})\}^{-1} \mathbf{B}_t^*(k_{ep}) \mathbf{c}_t \quad (12)$$

$$J(\hat{\mathbf{x}}(k_{ep}), k_{ep}) = -\mathbf{c}_t^* \mathbf{B}_t(k_{ep}) \{\mathbf{B}_t^*(k_{ep}) \mathbf{B}_t(k_{ep})\}^{-1} \mathbf{B}_t^*(k_{ep}) \mathbf{c}_t \quad (13)$$

### 2.3. Implementation

For efficient optimization, we used the Golden Section Search (GSS) technique [66], in which the minimum is found by sequentially narrowing the search range until reaching a prescribed tolerance. The GSS technique substantially reduces the number of iterations to find the minimum. An advantage of GSS is that given the viable range of search for the optimum parameter, the number of iterations is predictable based on the desired estimation resolution or tolerance [66]. Also, the one-dimensionality of the problem eliminates any uncertainty about the initialization of the optimization process. The search range need only encompass possible values of  $k_{ep}$ . For this work, the search range for  $k_{ep} = [0.03 - 6] \text{ min}^{-1}$  with tolerance of 0.0005 requires twelve iterations for VARPRO-based method. To match both methods, the LM iteration was stopped at twelve iterations as well and found to be adequate. We have used the magnitude of the MRI data for our patient studies and not the complex data.

The additional term in the ETM,  $v_p$ , must physiologically be a value between 0 and 1, and it is expected to be small, the order of 0.01. No constraints were placed on its estimation, and for LM  $v_p$  was initialized as 0.01.

### 2.4. Patient studies

The VP-based perfusion analysis described above was evaluated in numerical simulations as well as in human studies performed under a protocol approved by the Institutional Review Board. All enrolled subjects gave formal informed consent. All patients who met the following criteria were enrolled: (i) underwent the standard protocol for prostate MRI exam at 3 Tesla (Discovery MR750w, GE Healthcare, Milwaukee, WI), (ii) exam interpretation by one of the coauthors (ATF, five years experience in prostate MRI), (iii) subsequent histological evaluation of a prostate specimen after transrectal ultrasound-guided biopsy in either the 2nd or 4th quarter of 2016. This was a total of 20 subjects, 16 of which had subsequent radical prostatectomy. Patient characteristics are summarized in Table 1. Prostate adenocarcinoma was documented in 19 of the 20 patients after biopsy.

In all cases, an mpMRI exam was done, which included T2SE, DWI with DWI-derived apparent diffusion coefficient (ADC) map, and DCE-MRI sequences utilizing our institutional protocol. Relevant to this work are the acquisition parameters for the DCE-MRI sequence [67], summarized in Table 2, based on a 3D fast spoiled gradient-echo

(SPGR) acquisition [68] with view sharing [69]. Gadolinium based MR contrast agent (Dotarem, gadoterate meglumine, Guerbet, Roissy CdG, France) at a dose of 0.1 mmol/kg was administered intravenously at 3 ml/s followed by a 20 ml saline flush at 3 ml/s using a mechanical power injector. Signal reception was done using 32 coil elements, 16 in an anterior array and 16 in a posterior array.

For each case there were one or more foci of suspected prostate cancer depicted on mpMRI, and the index lesion was noted in the radiological report. The representative axial section containing this index lesion was selected for subsequent analysis. For all 31 time frames of the DCE-MRI acquisition, the MRI signals in the target section were converted to concentration of contrast material by using the SPGR signal model [70]. Specifically, using the SPGR and fast exchange model equations, as well as the imaging parameters, the MRI signal was mapped to concentration, assuming known  $T_{10}$  for blood and tissue (1600 ms, and 1597 ms), the contrast agent relaxivity,  $r_1$  ( $4.0 \text{ mM}^{-1} \text{ s}^{-1}$ ), and arterial maximum concentration (6 mM). The relative ratio between the arterial and tissue MRI signal was preserved. The resultant converted signals were then used for subsequent analysis. Ideally, the  $T_1$  relaxation times of the tissue and blood are estimated by  $T_1$ -mapping [43]. However, in this work the relaxivity,  $r_1$ , and pre-contrast,  $T_{10}$  value were assumed known from the literature [71]. The blood concentration curve vs. time was normalized for each individual by matching the area under the curve (first-pass) to the total concentration based on the weight of each patient. The blood volume was estimated as 5 L for a 70 kg man and extrapolated for lower or higher weights.

For each case the AIF,  $\mathbf{a}_t$  in the derivation, was selected from a  $3 \times 3$  voxel ROI chosen from within the lumen of the subject's left or right external iliac or proximal femoral artery in the same axial section as the dominant lesion. This is illustrated for one of the twenty patient studies in Fig. 1. Prior to this work we found that an ROI of this size provided good signal averaging across multiple pixels without contamination by edge effects at the lumen edge.

### 2.5. Comparison with Levenberg-Marquardt algorithm

The proposed VP-based parameter estimation, which entails solving a one-dimensional optimization problem, was compared with conventional multi-dimensional non-linear estimation based on the Levenberg-Marquardt (LM) method. Comparisons of accuracy and precision were performed as well as comparisons of the speed of convergence, i.e., the number of iterations and elapsed time from the onset of fitting until a stable cost function minimum value was achieved. All computations were performed using MATLAB (R2016a, The Mathworks, Natick, MA) on a Linux (CentOS 6.8)-based workstation with two E5-2670v2 CPUs (each with 10 cores at 2.5 GHz) and 64 GB of RAM.

#### 2.5.1. Accuracy and precision

To validate the accuracy and precision of VP-based perfusion estimation, a numeric simulation was developed as described schematically in the flowchart in Supporting Fig. S2. Thirty-one time frames with 6.6 s sampling were assumed, matching the clinical DCE-MRI protocol of Table 2. Tissue perfusion was simulated according to the TM with various assumed values of  $K^{trans}$  (0.1, 0.2, 0.3, and  $0.4 \text{ min}^{-1}$ ) and  $v_e$  (0.1, 0.2, and 0.3) that created a total of twelve combinations of ( $K^{trans}$ ,  $k_{ep} = K^{trans}/v_e$ ) that span those reported for normal and malignant tissue. Additionally for the ETM a  $v_p$  value of 0.01 was assumed. A population-based AIF was used [72].

Simulated MRI signals were then generated from these assumed tissue and arterial contrast concentration curves with the SPGR signal model. To approximate the statistical properties of the magnitude MR images that are typically obtained clinically, zero-mean Gaussian noise was added to the simulated signals (AIF and tissue) which were then converted back into concentration curves for perfusion analysis using both the VP and LM techniques. This was performed for all

**Table 1**  
Characteristics of patients used for evaluation of VARPRO-based estimation technique.

Case #	Age (year)	Weight (kg)	DCE-MRI frame time (s)	PSA at the time of mpMRI <sup>a</sup> (ng/mL)	Gleason score		Tumor description (number, location, size)
					Biopsy	RP <sup>b</sup>	
1	66	110	6.374	8.7	4 + 3	3 + 4	Single lesion/right superior-mid posterior/1.5 × 1.1 × 0.5 cm
2	64	73	6.597	11.0	4 + 3	4 + 3	Dominant lesion/posterior right peripheral zone/1.0 × 0.8 × 0.4 cm
3	59	75	6.768	3.0	3 + 3	3 + 3	Single lesion/right posterior/base/extruded BPH nodule at the prostate base/0.4 cm
4	57	87	6.781	9.5	3 + 4	3 + 4	Multifocal/left superior posterior/Left dominant peripheral zone/0.9 × 0.5 × 0.4 cm
5	69	82	6.087	20.5	4 + 4	3 + 4	Multifocal/Left peripheral zone/dominant nodule, in left anterior inferior to left posterior superior/0.6 × 0.4 × 0.4 cm
6	62	88	6.659	5.9	Benign	NP <sup>c</sup>	No evidence of malignancy at biopsy.
7	75	92	7.073	6.0	3 + 3	NP <sup>c</sup>	Midline posterior peripheral zone/needle biopsy
8	64	70	5.836	5.3	3 + 3	NP <sup>c</sup>	Left apex/needle biopsy
9	71	85	6.630	4.8	3 + 3	NP <sup>c</sup>	Bilateral/dominant right peripheral zone/needle biopsy
10	68	86	5.295	6.5	3 + 3	3 + 4	Multifocal/dominant lesion right anterior prostate/2.3 × 1.8 × 1.1 cm/Multiple tumor foci left posterior prostate
11	64	82	6.592	7.7	4 + 3	4 + 3	Single lesion/left anterior mid prostate/1.0 × 0.5 × 0.4 cm
12	60	75	6.380	7.8	4 + 3 (R)	4 + 3	Two lesions/right mid inferior posterior prostate/1.3 × 1.1 × 0.8 cm/left superior mid posterior prostate/1.4 × 1.2 × 0.5 cm
13	67	111	6.369	4.7	3 + 4	3 + 4	Single tumor/right posterior/2.4 × 1.2 × 1.0 cm
14	71	84	6.329	6.5	4 + 3 (L)	3 + 4	Two lesions/left superior mid anterior posterior prostate/1.2 × 0.8 × 0.6 cm/right superior mid inferior anterior posterior prostate/1.1 × 1.1 × 0.9 cm
15	64	153	5.640	8	3 + 4	3 + 4	Multifocal/posterior aspect of right and left prostatic lobes
16	59	82	6.340	21.4	4 + 4	Benign	Prostatectomy revealed benign prostatic tissue with scattered foamy histiocytic aggregates, consistent with positive response to neoadjuvant androgen deprivation therapy (ADT). Note mpMRI of the prostate was performed prior to ADT.
17	67	84	6.448	13.4	3 + 4(L)/3 + 3(R)	4 + 3	Two lesions/left and right lobes/1.8 and 0.7 cm
18	70	71	6.231	4.8	3 + 3	3 + 4	Single lesion/left posterior/1.2 × 0.8 × 0.8 cm
19	56	98	6.099	5.3	4 + 4	3 + 4	Single lesion/involved right and left prostate/2.6 × 1.6 × 1.0 cm
20	60	111	6.395	19.9	3 + 4	3 + 4	Single lesion/left prostate/1.5 × 1.5 × 1.4 cm

<sup>a</sup> mpMRI = multi-parametric MRI.

<sup>b</sup> RP = radical prostatectomy.

<sup>c</sup> NP = not performed.

**Table 2**  
Typical imaging parameters for DCE-MRI.

TR (repetition time)	5.3 ms <sup>a</sup>
TE (echo time)	2.2 ms <sup>a</sup>
Sampling resolution <sup>b</sup> (in-plane matrix) × slice	256 × 384 × 38
Field of view <sup>b</sup>	220 × 442 × 114 mm <sup>3</sup>
Spatial resolution <sup>b</sup>	0.86 × 1.15 × 3.0 mm <sup>3</sup>
Acceleration	R <sub>y</sub> 2.49
	R <sub>z</sub> 1.12
Bandwidth	± 62.5 kHz
Flip angle	12°
Scan time	~4 min <sup>a</sup>
Frame time	6.6 s <sup>a</sup>
Temporal footprint	19 s <sup>a</sup>

<sup>a</sup> May change slightly depending on body habitus.

<sup>b</sup> Expressed as anterior/posterior (A/P) × left/right (L/R) × superior/inferior (S/I), corresponding to frequency × phase × slice encode directions.

combinations and for each of six different signal to noise ratio (SNR) levels which spanned those observed in our patient studies.

For this work the noise added to the simulated MR signal was expressed as a fraction of the peak signal enhancement over the time series. To relate this to that observed clinically, the standard deviation,  $\sigma$ , was measured in an ROI within an enhancing region of the prostate of a difference image [73] made between consecutive DCE-MRI images near the end of the 31-frame acquisition; i.e. having negligible frame-to-frame change in mean signal. The SNR was then defined as the highest mean signal enhancement of that ROI over the unsubtracted time series divided by  $\sigma/\sqrt{2}$ . This was performed for ten consecutive DCE-MRI prostate studies acquired similarly to those of Table 1 and having suspicious enhancing lesions. SNR values measured with this approach ranged from 16 to 31. The analogous SNR levels used in the simulation were chosen to encompass this range and ranged from 10 to 35.

For each estimation method (VP and LM), for each ( $K^{trans}$ ,  $k_{ep}$ ) or ( $K^{trans}$ ,  $k_{ep}$ ,  $v_p$ ) combination, and for each assumed SNR level, Monte Carlo simulation was performed 500 times for both TM and ETM. The resultant estimated perfusion parameters were then tabulated.

### 2.5.2. Convergence

To compare the speed of convergence of VP with LM, perfusion analysis was performed using the patient data. For each patient, ten voxels were selected by a radiologist coauthor (AK, > 20 years experience in prostate MRI) from the axial section previously identified: five pixels from within the index lesion and five from normal tissue, typically from the same zone of the prostate as the malignant tissue but on the contralateral side. The mean time per iteration was noted in performing the fit for each voxel for both the VP and LM methods. This was done by executing each method 100 times and determining the average computation time. Next, for each voxel the full estimation process was performed and the residual determined after each iteration, where the residual is defined as the root-mean-square (RMS) deviation of the difference between the estimated and acquired perfusion signals. The residual was plotted separately vs. the absolute cumulative computation time. The estimated  $K^{trans}$  and  $k_{ep}$  values were noted.

For each voxel the LM estimation processes were initialized with a starting ( $K^{trans}$ ,  $k_{ep}$ ) randomly selected from the range of [0.05–2] min<sup>-1</sup> for both TM and ETM, and the additional term in ETM,  $v_p$  was initialized with 0.01. The VP optimization process, which does not need an initial guess, searches the range of [0.03–6] min<sup>-1</sup> for  $\hat{k}_{ep}$  using GSS as described.

## 3. Results

The fitting performed using our VARPRO-based strategy is illustrated in Fig. 2. Fig. 2a–b show examples of the cost function,  $J$ , (Eq.

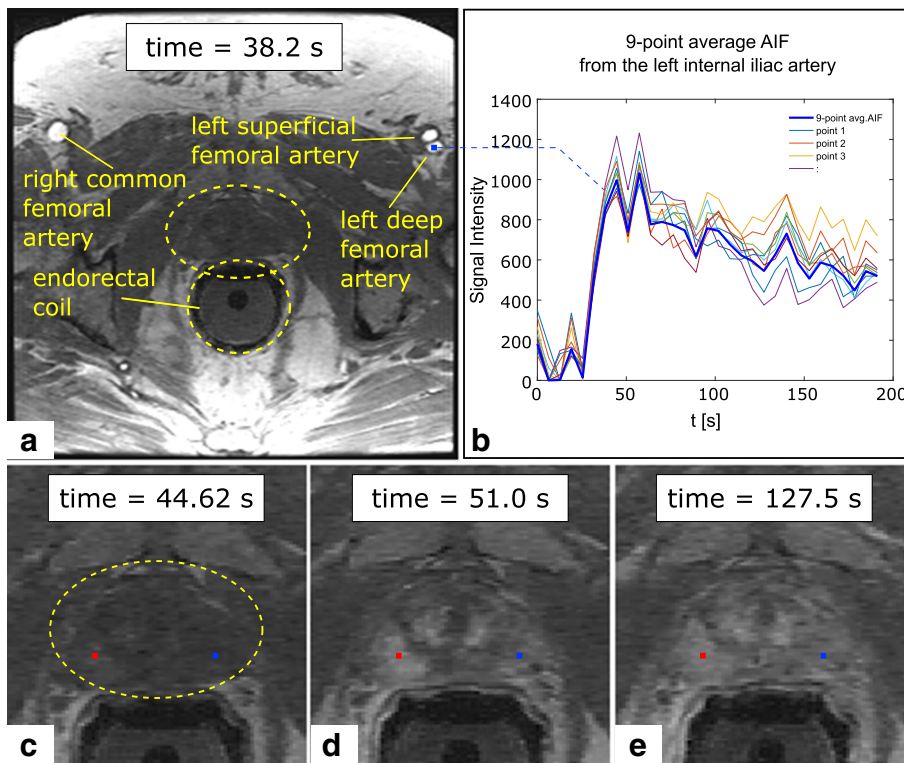


Fig. 1. (a) Axial slice of the pelvis (Patient #1) through the prostate showing the bilateral femoral arteries, prostate (within yellow oval) and endo-rectal coil (yellow circle, not active for DCE-MRI sequence). The arteries are enhanced at time 38.2 s post-injection. (b) Graph of the average (bold curve) arterial input function selected from the left deep femoral artery as shown. The average is from nine ( $3 \times 3$ ) individual voxels (non-bold curves). (c–e) Source DCE-MRI images demonstrate an area of hyperenhancement of cancerous tissue in the right peripheral zone at the apex compared to the non-cancerous tissue in the contralateral side at times 44.6 s (c), 51.0 s (d), and 127.5 s (e). Red and blue points show the representative voxels in the cancer and non-cancerous regions respectively. These are used in Fig. 2. (For interpretation of the references to colour in this figure legend, the reader is referred to the web version of this article.)

(8) plotted vs.  $k_{ep}$  for two representative voxels from cancerous (a) and normal (b) tissue selected from the study shown in Fig. 1 (red and blue points). In each case  $\hat{k}_{ep}$  is selected as that corresponding to the minimum of  $J$ , and  $\hat{K}^{trans}$  is then calculated via Eq. (6). The resultant

estimated tissue perfusion signals,  $p_b$ , generated using the calculated  $\hat{K}^{trans}$  and  $\hat{k}_{ep}$  values (dashed lines) are plotted vs. time and compared to the acquired perfusion data (solid lines),  $c_b$ , in Fig. 2c for both the cancerous (red) and normal (blue) tissues.

Fig. 3 shows box-and-whisker plots which compare the VP and LM

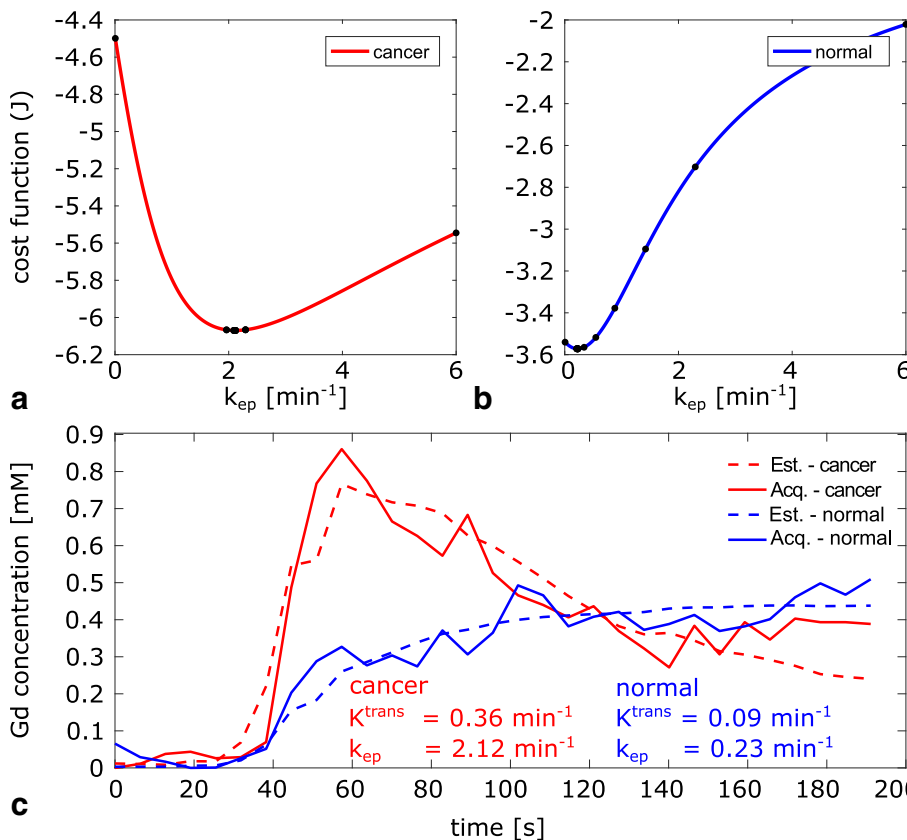
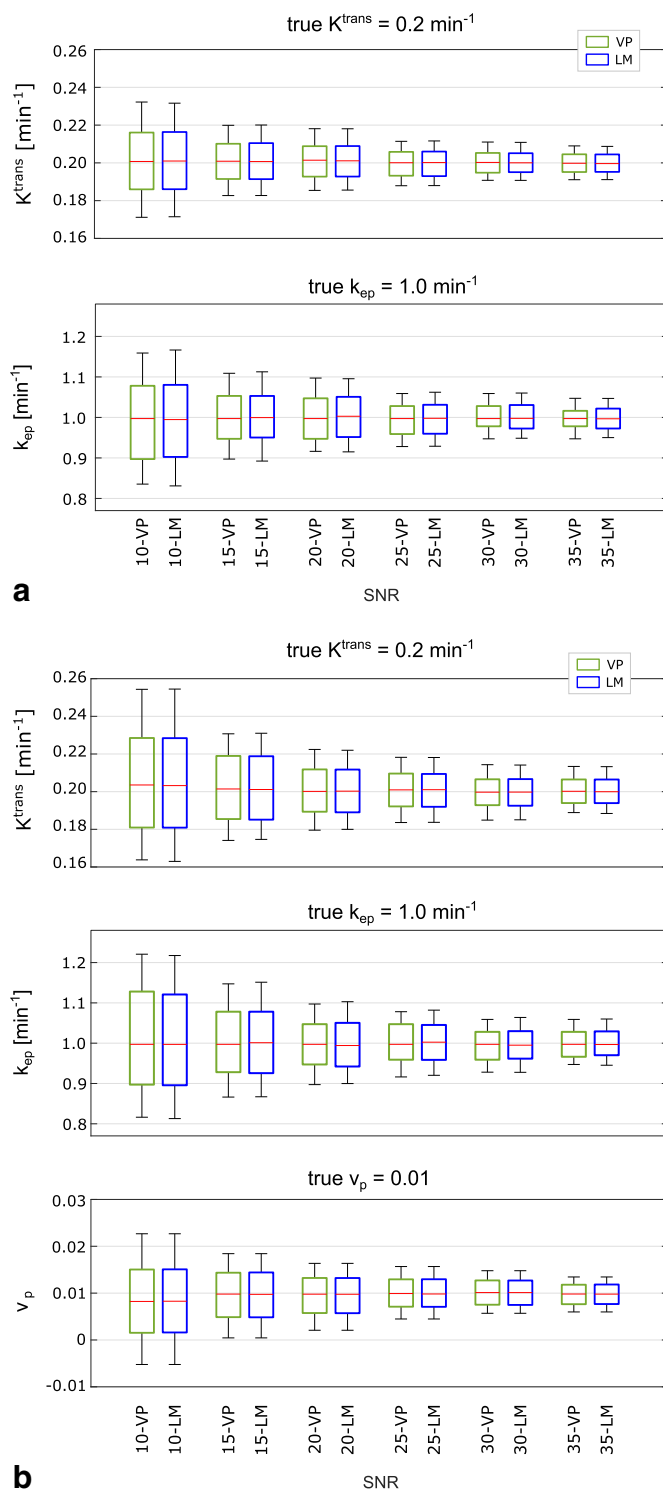


Fig. 2. Cost function ( $J$ ) vs.  $k_{ep}$  shown for one voxel in (a) the cancerous region (red line) and one voxel in (b) the non-cancerous region (blue line) in the same patient shown in Fig. 1. Black dots correspond to points selected each iteration by Golden Section Search (GSS) method. (c) Estimated perfusion (dashed line) vs. acquired perfusion (solid line) for the two representative voxels shown in Fig. 1c–e. The optimum  $k_{ep}$  values (cost function minimum) found via GSS method and the subsequently computed  $K^{trans}$  are indicated. (For interpretation of the references to colour in this figure legend, the reader is referred to the web version of this article.)



**Fig. 3.** The results of the numeric simulation using Monte Carlo simulation.  $K^{trans}$  (top) and  $k_{ep}$  (bottom) box-and-whisker plots are depicted for VP and LM for six SNR levels (10, 15, 20, 25, 30, 35). The boxes depict the median, first and third quartiles and the whiskers mark the 10th and 90th percentiles across 500 Monte Carlo samples for the specific combination of  $K^{trans} = 0.2 \text{ min}^{-1}$ ,  $k_{ep} = 1.0 \text{ min}^{-1}$ ,  $v_p = 0.01$ . Fig. 3a,b show the results for Tofts and extended Tofts model respectively.

estimation methods for a range of assumed SNR levels for the specific case of ( $K^{trans} = 0.2 \text{ min}^{-1}$ ,  $k_{ep} = 1.0 \text{ min}^{-1}$ ,  $v_p = 0.01$  (for ETM)), for both perfusion models, TM (a) and ETM (b). A summary of results for TM over all of the combinations considered is presented in Supporting Tables S1, S2. The summary of results for ETM is similar and not

presented for brevity.

Results illustrating the convergence process for VP vs. LM are shown in Supporting Fig. S3a–b for Tofts and extended Tofts model respectively. In this figure the ten selected points from Patient #4 were used to demonstrate the convergence process. Five points from the dominant lesion were shown on top and five points from the normal region at the bottom. Each plot shows the results for VP (blue) and LM (red). The plots are representative of those seen for all ten patient studies.

Fig. 4a compares the computation times required to attain convergence for the first ten patient studies, with results for Patients #1 to #5 in the first row and #6 to #10 in the second row. Each plot is comprised of comparisons of VP with LM for each of the ten points selected for that patient. For all 100 points in these ten patient cases VP converged. As indicated on top of each plot, in some cases the LM failed to converge, e.g. one point in Patient #2, and these were excluded from the plots. The quantization of times along the abscissa is due to the discrete computation time per iteration for each method. Fig. 4b shows the same results for the ETM.

Fig. 4c shows the combination of all of the computation time data of Fig. 4a,b. Of the 100 points analyzed (ten for each patient) a total of 15 for TM (14 for ETM) failed to converge using the LM method. Box-and-whisker plots of the remaining 85 (86 for ETM) comparisons are shown. The mean values using the TM were 0.244 ms for LM and 0.079 ms for VP, and the ratio ( $0.244/0.079 = 3.08$ ) is taken as the average speed-up in computation time provided by VP. The equivalent numbers for ETM are: LM = 0.477 ms, VP = 0.263 ms, ratio =  $0.477/0.263 = 1.8$ . Similar results to those in Fig. 4 were found for Patients #11–#20. In aggregate, for Patients, #1 - #20 LM failed to converge for the Tofts model for 29 of the 200 points analyzed (14.5%). 7/29 (24.1%) of the failed points occurred in cancerous tissue and 22/29 (75.9%) in normal tissue. Similar results were found for LM for the Extended Tofts Model. The VP method successfully converged for 200/200 points (100%) for both models.

Fig. 5 summarizes the results in all twenty patients. Fig. 5a is a summary presentation of the estimated  $K^{trans}$  pharmacokinetic parameters for all voxels analyzed from the twenty patient studies using the VP method for TM and ETM. Fig. 5b shows the ROC curve using the pathology results from biopsy and prostatectomy as the standard and calculated based on  $K^{trans}$  for TM (solid line) and ETM (dashed line). Fig. 5c,d shows the same results for  $k_{ep}$ . The cut-off values for  $K^{trans}$  and  $k_{ep}$ , sensitivity, specificity and area under the curve (AUC) are noted on the figure.

Results from mpMRI exams that include T2SE, ADC map, and the VARPRO-based perfusion maps are shown for two representative patients in Fig. 6 and Fig. 7. No artifact related to the VARPRO technique was observed in any of 20 clinical patients.

#### 4. Discussion

In this work we have demonstrated how the Variable Projection (VARPRO) approach can be used to computationally simplify and improve the reliability of non-linear least squares (NLLS) estimation of the Tofts and extended Tofts model for determining pharmacokinetic parameters,  $K^{trans}$  and  $k_{ep}$ , (and  $v_p$ ) from 4D DCE-MRI data. NLLS estimation of perfusion parameters using our VARPRO-based optimization strategy is fundamentally more efficient than alternative NLLS fitting techniques because the search is performed only across one dimension as opposed to throughout a two or three-dimensional space. In our numerical implementation, this strategy enabled an approximate  $5 \times$  reduction in computation time per iteration (as seen in Figs. S2 and Fig. 4) and  $3 \times$  reduction in overall fitting time for TM and  $2 \times$  reduction for ETM.

The robustness of the perfusion estimation through noise was evaluated with a numeric simulation in which true perfusion values were assumed and noise was added to the simulated MR signals. The SNR levels used in the simulation and the assumed  $K^{trans}$ ,  $k_{ep}$ , and  $v_p$

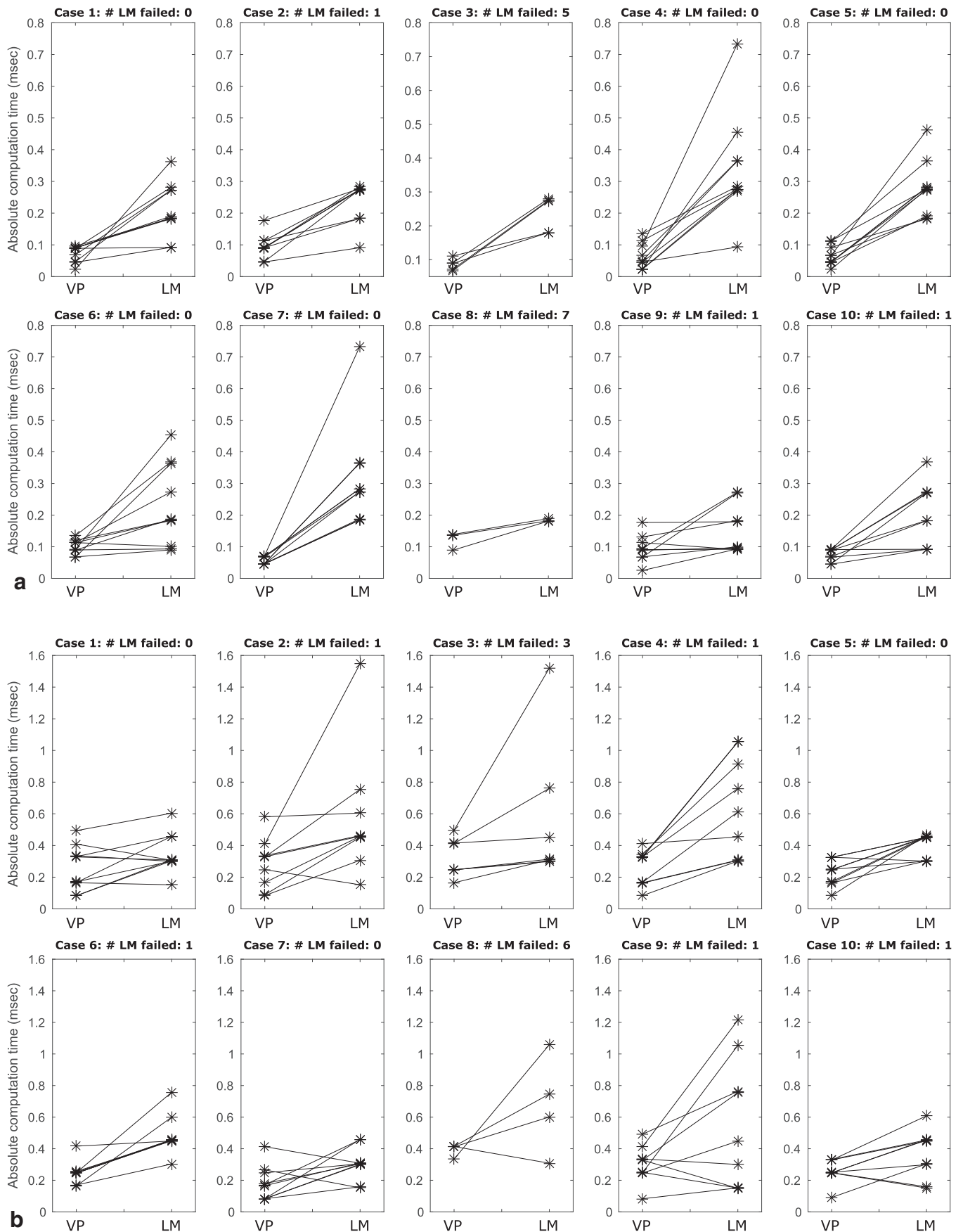


**Fig. 4.** (a) Absolute computation time for convergence for each point (total of ten points for each patient) shown for VP and LM using the Tofts model. The VP-based method converged for all 100 points. At the top of each plot, the number of points (out of ten) that failed for LM method is noted. The failed points are not shown in the plots. (b) the equivalent plots for the extended Tofts model. (c) Absolute computation time for convergence for all the analyzed points in (a,b). 15 out of 100 points failed to converge for the LM method using the Tofts model and 14 failed using the extended Tofts model. Box-and-whisker plots depict median (dashed line), mean (solid line), first and third quartiles, and 10th and 90th percentiles.

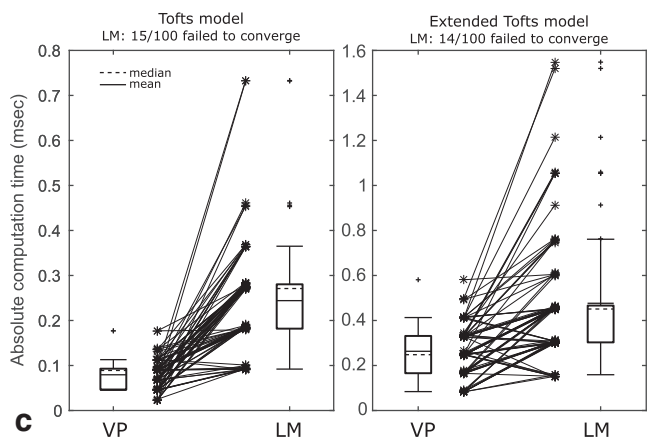


Fig. 4. (continued)

values spanned those found to be typical in prostate DCE-MRI patient studies from our institution. As demonstrated through numeric simulation, VP-based perfusion parameter estimation exhibits comparable accuracy and precision to the standard LM algorithm for a broad range of SNR levels, assuming the LM technique is properly initialized and

appropriately terminated. If the LM method is initialized far from the optimum value, for this problem class, the optimization process was commonly observed to fall into suboptimal local minima.

Both VP and LM algorithms have more computation burden for the ETM compared to TM. This is expected due to the more involved computations at each iteration. However, for the VP technique, the computational advantage is less because for TM the term being inverted is a scalar (Eq. (8)) but in Eq. (13), it is a matrix. Thus a bigger step for VP and that is why the speed ratio changes from 3 to 1.8.

The clinical applicability of the VARPRO-based technique was shown by generating perfusion maps from 3D DCE-MRI image sequences from 20 subjects with known or highly suspected prostate cancer. In the patient studies, the LM method failed to converge in 29/200 points (14.5%) for the TM fitting and 30/200 (15%) for ETM fitting. Almost one quarter of these failures were in points within cancer and the remainder in the contralateral normal tissue. On the other hand, the VP-based optimization successfully converged in 200/200 (100%) of the points for both TM and ETM fitting. This ideal performance realized by VP is desirable in any clinical test (including prostate DCE-MRI) where the presence and location of cancer are typically not known prior to the exam. Eliminating technical failure (in this case a failure to converge) is one of the earliest necessary steps in showing efficacy of a possible new clinical test [74].

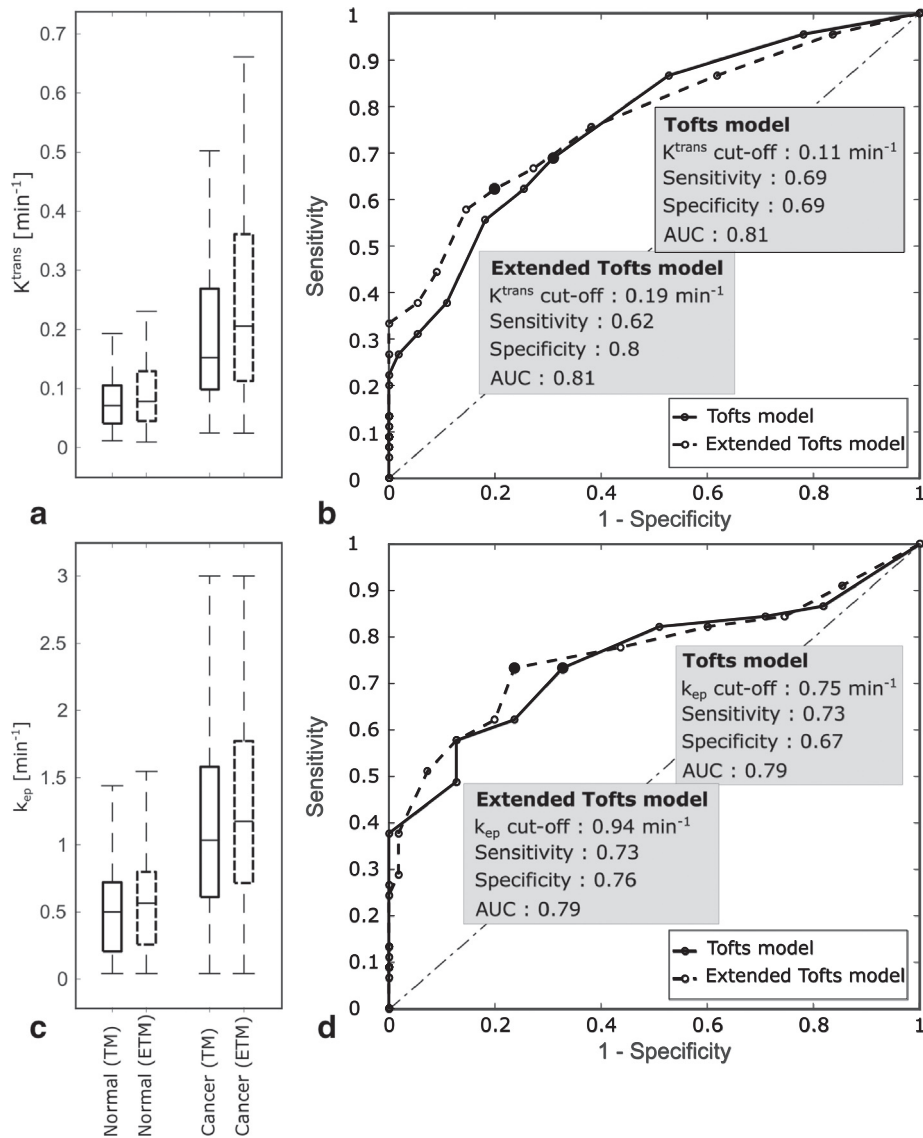
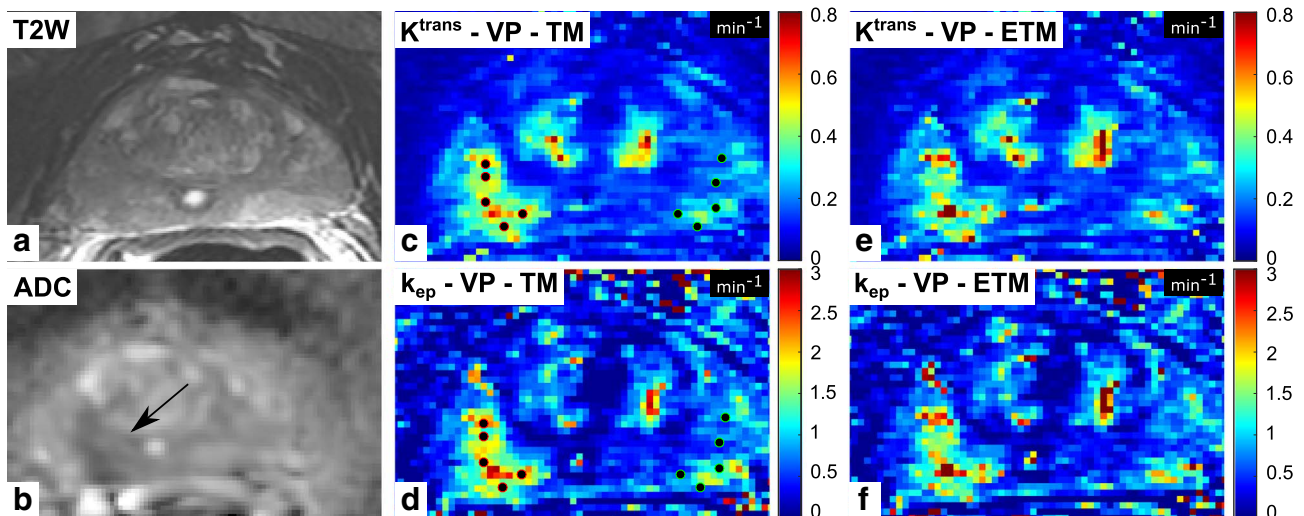


Fig. 5. (a) The  $K^{trans}$  range estimated for normal and cancer region in twenty patients for Tofts and extended Tofts model via the VARPRO technique. (b) The ROC curve based on  $K^{trans}$ , for Tofts and extended Tofts model. The equivalent information for  $k_{ep}$  is shown in (c,d). The cut-off values (solid dot on the ROC curve), sensitivity, specificity, and the AUC are noted on the figures (b,d) for TM and ETM.



**Fig. 6.** 66-year-old male (Patient #1) with PSA of 8.7 ng/ml. Prostate biopsy revealed adenocarcinoma, Gleason 4 + 3 = 7 on the right and benign tissue on the left.: (a)  $T_2$ -weighted spin echo (T2SE) image, and (b) apparent diffusion coefficient (ADC) map demonstrate an ill-defined heterogeneous tumor of hypointensity in the right posterolateral peripheral zone at the mid gland (b, arrow). (c–f) Corresponding perfusion abnormality is comparably shown on  $K^{trans}$  and  $k_{ep}$  maps from VARPRO (VP) using Tofts model (TM) and extended Tofts model (ETM). The 10 representative points used for computation speed comparisons, are shown in the major tumor and the contralateral side in (c) and (d).

As described in the **Introduction**, the VARPRO technique can be applied to the group of non-linear least squares problems that are separable and have a linear combination of non-linear and/or linear terms. Conceivably this technique could be used to reduce the dimensionality of the search for optimum parameters for other models of perfusion using DCE-MRI data; e.g [34].

This work does have limitations. One of these is the lack of subject- and system-specific  $T_1$ - and  $B_1^+$ -mapping (i.e., RF flip angle) before contrast injection. Doing so would provide patient-specific, pre-contrast  $T_1$  values and improve the accuracy and precision with which MR signal is converted to concentration. However, many of the findings presented here, such as the basic derivation and simulation studies, did not rely on this conversion process. Another limitation is that motion correction was not used in the VARPRO-based analysis, but motion did not seem problematic in any of the 20 cases. Also, the VP method could conceivably have been compared with other estimation methods. For NLLS this could have been, for example, a trust-region-based approach [33,75]. However, this is still a multi-dimensional optimization, like LM is dependent on the initialization,

and has been shown to have problems in convergence similar to LM [33]. Detailed comparison with LLSQ was considered to be beyond the scope of this work. Finally, the relatively low number of patient studies, 20 in this case, is limiting from a statistical power standpoint. However, these were used simply to show the applicability of the VARPRO-based method to prostate DCE-MRI data of known cancer. A larger number would be warranted for any studies of sensitivity, specificity, or accuracy.

In summary, we have shown mathematically how the Variable Projection (VP) approach can be applied to non-linear least squares estimation of perfusion parameters from a time series of DCE-MR images for both the Tofts and Extended Tofts models. The conversion of the problem to a one-dimensional optimization simplifies the search and initialization. Compared to the standard Levenberg-Marquardt method the VP approach provides similar accuracy and noise sensitivity, approximately three-fold reduced computation time, and 100% reliability in convergence in both cancerous and non-cancerous tissues.

Supplementary data to this article can be found online at <https://doi.org/10.1016/j.mri.2017.12.021>.

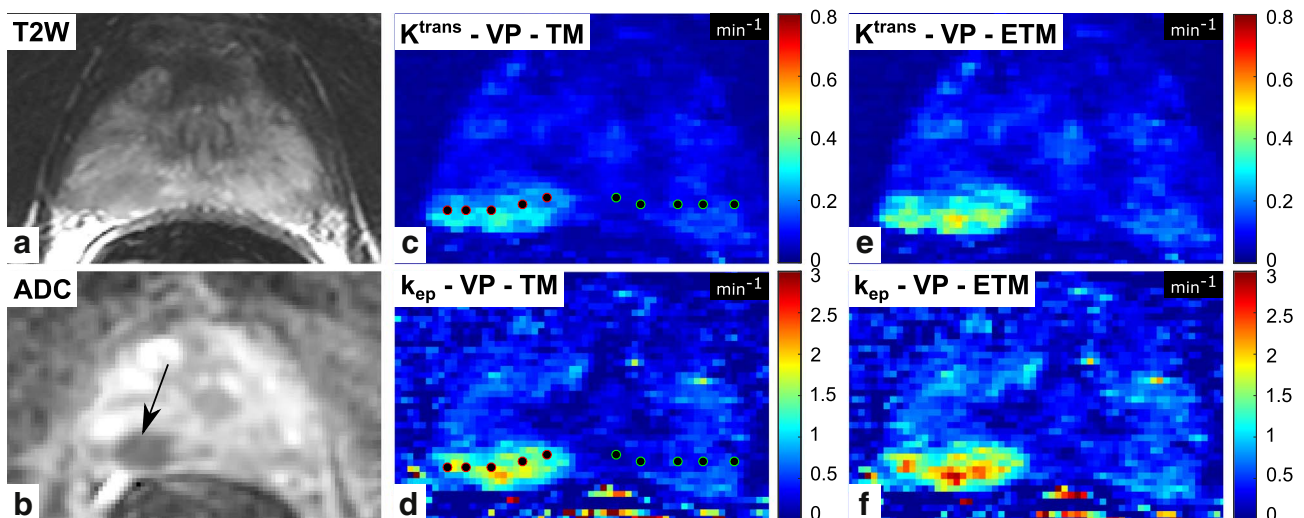


**Fig. 7.** 64-year-old male (Patient #2) with PSA of 11 ng/mL.: (a)  $T_2$  signal abnormalities and (b) diffusion restriction (ADC map) in the right posterior peripheral zone (b, arrow). (c,e)  $K^{trans}$  and (d,f)  $k_{ep}$  maps from VARPRO (VP) using Tofts model (TM) and extended Tofts model (ETM), reveal hyperenhancing lesion in the right posterolateral peripheral zone. The 10 representative points used for computation speed comparisons are shown in the major tumor and the contralateral side in (c) and (d). Prostate biopsy yielded adenocarcinoma, Gleason score 4 + 3 = 7 disease on the right.

## Acknowledgments

Clinic Discovery Translation Program, and from NIH [grant number EB000212, RR018898], and DOD [grant number W81XWH-15-1-0341].

Support is acknowledged from Mayo Graduate School, the Mayo

## Appendix A

Here the steps to derive Eq. (6) from Eq. (5) are shown. Eq. (5) is repeated as Eq. (A.1)

$$J(K^{trans}, k_{ep}) = \|\mathbf{p}_t - \mathbf{c}_t\|_2^2 = \|\mathbf{A}\mathbf{h}_t(k_{ep})K^{trans} - \mathbf{c}_t\|_2^2 = \|\mathbf{b}_t(k_{ep})K^{trans} - \mathbf{c}_t\|_2^2 \quad (\text{A.1})$$

where  $\mathbf{b}_t(k_{ep}) = \mathbf{A}\mathbf{h}_t(k_{ep})$  Eq. (A.1) can be expanded to:

$$\begin{aligned} J(K^{trans}, k_{ep}) &= (\mathbf{b}_t(k_{ep})K^{trans} - \mathbf{c}_t)^*(\mathbf{b}_t(k_{ep})K^{trans} - \mathbf{c}_t) \\ &= ((K^{trans})^*\mathbf{b}_t^*(k_{ep}) - \mathbf{c}_t^*)(\mathbf{b}_t(k_{ep})K^{trans} - \mathbf{c}_t) \\ &= (K^{trans})^*\mathbf{b}_t^*(k_{ep})\mathbf{b}_t(k_{ep})K^{trans} - (K^{trans})^*\mathbf{b}_t^*(k_{ep})\mathbf{c}_t \\ &\quad - \mathbf{c}_t^*\mathbf{b}_t(k_{ep})K^{trans} + \mathbf{c}_t^*\mathbf{c}_t \end{aligned} \quad (\text{A.2})$$

To minimize  $J$ , the cost function is differentiated with respect to  $(K^{trans})^*$  and set to zero:

$$\nabla_{(K^{trans})^*}(J) = \mathbf{b}_t^*(k_{ep})\mathbf{b}_t(k_{ep})K^{trans} - \mathbf{b}_t^*(k_{ep})\mathbf{c}_t = 0 \quad (\text{A.3})$$

Solving for  $K^{trans}$  gives the optimum value,  $\widehat{K}^{trans}$ , as a function of  $k_{ep}$ :

$$\widehat{K}^{trans} = \{\mathbf{b}_t^*(k_{ep})\mathbf{b}_t(k_{ep})\}^{-1}\mathbf{b}_t^*(k_{ep})\mathbf{c}_t \quad (\text{A.4})$$

which is Eq. (6) in the text. The final expression for the cost function, Eq. (8), is developed by inserting the expression for  $\widehat{K}^{trans}$  from Eq. (A.4) into Eq. (A.1) leading to:

$$\begin{aligned} J(\widehat{K}^{trans}(k_{ep}), k_{ep}) &= \|\mathbf{b}_t(k_{ep})\widehat{K}^{trans} - \mathbf{c}_t\|_2^2 \\ &= \|\mathbf{b}_t(k_{ep})\{\mathbf{b}_t^*(k_{ep})\mathbf{b}_t(k_{ep})\}^{-1}\mathbf{b}_t^*(k_{ep})\mathbf{c}_t - \mathbf{c}_t\|_2^2 \end{aligned} \quad (\text{A.5})$$

For brevity  $\mathbf{b}_t(k_{ep})$  is shown as  $\mathbf{b}_t$  in the remainder of the derivation. Eq. (A.5) can be expanded to:

$$\begin{aligned} J(\widehat{K}^{trans}(k_{ep}), k_{ep}) &= (\mathbf{b}_t\{\mathbf{b}_t^*\mathbf{b}_t\}^{-1}\mathbf{b}_t^*\mathbf{c}_t - \mathbf{c}_t)^*(\mathbf{b}_t\{\mathbf{b}_t^*\mathbf{b}_t\}^{-1}\mathbf{b}_t^*\mathbf{c}_t - \mathbf{c}_t) \\ &= (\mathbf{c}_t^*\mathbf{b}_t\{\{\mathbf{b}_t^*\mathbf{b}_t\}^{-1}\}^*\mathbf{b}_t^* - \mathbf{c}_t^*)(\mathbf{b}_t\{\mathbf{b}_t^*\mathbf{b}_t\}^{-1}\mathbf{b}_t^*\mathbf{c}_t - \mathbf{c}_t) \\ &= \mathbf{c}_t^*\mathbf{b}_t\{\{\mathbf{b}_t^*\mathbf{b}_t\}^{-1}\}^*\mathbf{b}_t^*\mathbf{b}_t\{\mathbf{b}_t^*\mathbf{b}_t\}^{-1}\mathbf{b}_t^*\mathbf{c}_t - \mathbf{c}_t^*\mathbf{b}_t\{\{\mathbf{b}_t^*\mathbf{b}_t\}^{-1}\}^*\mathbf{b}_t^*\mathbf{c}_t \\ &\quad - \mathbf{c}_t^*\mathbf{b}_t\{\mathbf{b}_t^*\mathbf{b}_t\}^{-1}\mathbf{b}_t^*\mathbf{c}_t + \mathbf{c}_t^*\mathbf{c}_t \end{aligned} \quad (\text{A.6})$$

Upon noting in the first term that  $\mathbf{b}_t^*\mathbf{b}_t\{\mathbf{b}_t^*\mathbf{b}_t\}^{-1}$  equals unity, the first and second terms of Eq. (A.6) cancel, resulting in:

$$J(\widehat{K}^{trans}(k_{ep}), k_{ep}) = -\mathbf{c}_t^*\mathbf{b}_t\{\mathbf{b}_t^*\mathbf{b}_t\}^{-1}\mathbf{b}_t^*\mathbf{c}_t + \mathbf{c}_t^*\mathbf{c}_t \quad (\text{A.7})$$

Because  $\mathbf{c}_t^*\mathbf{c}_t$  is independent of  $k_{ep}$  it can be dropped for the optimization, resulting in Eq. (8).

## Appendix B

The VARPRO technique can similarly be applied to the extended Tofts Model (ETM). Starting with Eq. (10) from the text, repeated here as Eq. (B.1)

$$\mathbf{p}_t = \mathbf{a}_t v_p + \mathbf{A}\mathbf{h}_t(k_{ep})K^{trans} = [\mathbf{a}_t \quad \mathbf{A}\mathbf{h}_t(k_{ep})] \begin{bmatrix} v_p \\ K^{trans} \end{bmatrix} = \mathbf{B}_t(k_{ep})\mathbf{x} \quad (\text{B.1})$$

The cost function  $J$  is then:

$$J(K^{trans}, k_{ep}, v_p) = \|\mathbf{p}_t - \mathbf{c}_t\|_2^2 = \|\mathbf{B}_t(k_{ep})\mathbf{x} - \mathbf{c}_t\|_2^2 \quad (\text{B.2})$$

which can be expanded (similar to Eq. (A.2)) to the expression shown here:

$$J(\mathbf{x}, k_{ep}) = \mathbf{x}^*\mathbf{B}_t^*\mathbf{B}_t\mathbf{x} - \mathbf{x}^*\mathbf{B}_t^*\mathbf{c}_t - \mathbf{c}_t^*\mathbf{B}_t\mathbf{x} + \mathbf{c}_t^*\mathbf{c}_t \quad (\text{B.3})$$

where  $\mathbf{B}_t(k_{ep})$  is shown as  $\mathbf{B}_t$  for brevity. The only difference vs. Eq. (A.2) is that  $\mathbf{x}$  is a vector replacing  $K^{trans}$  and  $\mathbf{B}_t$  is a matrix replacing vector  $\mathbf{b}_t$ . To minimize  $J$ , the cost function is differentiated with respect to  $\mathbf{x}^*$  and set to zero:

$$\nabla_{\mathbf{x}^*}(J) = \mathbf{B}_t^*\mathbf{B}_t\mathbf{x} - \mathbf{B}_t^*\mathbf{c}_t = 0 \quad (\text{B.4})$$

Solving for  $\mathbf{x}$  gives the optimum value,  $\widehat{\mathbf{x}}$ , as a function of  $k_{ep}$ :

$$\widehat{\mathbf{x}} = \{\mathbf{B}_t^*\mathbf{B}_t\}^{-1}\mathbf{B}_t^*\mathbf{c}_t \quad (\text{B.5})$$

Insertion into Eq. (B.2), expansion, and simplification similar to that in Appendix A leads to the final expression for the cost function, dependent only on the single variable  $k_{ep}$ , and the final term  $\mathbf{c}_t^*\mathbf{c}_t$  is dropped to form Eq. (13) in the text.

$$J(\widehat{\mathbf{x}}(k_{ep}), k_{ep}) = -\mathbf{c}_t^*\mathbf{B}_t\{\mathbf{B}_t^*\mathbf{B}_t\}^{-1}\mathbf{B}_t^*\mathbf{c}_t + \mathbf{c}_t^*\mathbf{c}_t \quad (\text{B.6})$$

The optimum value for  $k_{ep}$ , can be found by line search and then used in Eq. (B.5) to calculate the optimum  $K^{trans}$ ,  $v_p$  that are imbedded in  $\widehat{\mathbf{x}}$ .

## References

- [1] Leach MO, Brindle KM, Evelhoch JL, Griffiths JR, Horsman MR, Jackson A, et al. The assessment of antiangiogenic and antivascular therapies in early-stage clinical trials using magnetic resonance imaging: issues and recommendations. *Br J Cancer* 2005;92:1599–610.
- [2] Larsson HB, Stubgaard M, Frederiksen JL, Jensen M, Henriksen O, Paulson OB. Quantitation of blood-brain barrier defect by magnetic resonance imaging and gadolinium-DTPA in patients with multiple sclerosis and brain tumors. *Magn Reson Med* 1990;16:117–31.
- [3] Brix G, Semmler W, Port R, Schad LR, Layer G, Lorenz WJ. Pharmacokinetic parameters in CNS Gd-DTPA enhanced MR imaging. *J Comput Assist Tomogr* 1991;15:621–8.
- [4] Tofts PS, Brix G, Buckley DL, Evelhoch JL, Henderson E, Knopp MV, et al. Estimating kinetic parameters from dynamic contrast-enhanced T1-weighted MRI of a diffusible tracer: standardized quantities and symbols. *J Magn Reson Imaging* 1999;10:223–32.
- [5] Tofts PS, Kermode AG. Measurement of the blood-brain barrier permeability and leakage space using dynamic MR imaging. 1. Fundamental concepts. *Magn Reson Med* 1991;17:357–67.
- [6] Tofts PS. Modeling tracer kinetics in dynamic Gd-DTPA MR imaging. *J Magn Reson Imaging* 1997;7:91–101.
- [7] Padhani AR, Leach MO. Antivascular cancer treatments: functional assessments by dynamic contrast-enhanced magnetic resonance imaging. *Abdom Imaging* 2005;30:325–42.
- [8] Schmid VJ, Whitcher B, Padhani AR, Taylor NJ, Yang G-Z. Bayesian methods for pharmacokinetic models in dynamic contrast-enhanced magnetic resonance imaging. *IEEE Trans Med Imaging* 2006;25:1627–36.
- [9] Fütterer JJ, Heijmink SWTPJ, Scheenen TWJ, Veltman J, Huisman HJ, Vos P, et al. Prostate cancer localization with dynamic contrast-enhanced MR imaging and proton MR spectroscopic imaging. *Radiology* 2006;241:449–58.
- [10] Sourbron SP, Buckley DL. On the scope and interpretation of the Tofts models for DCE-MRI. *Magn Reson Med* 2011;66:735–45.
- [11] Bonekamp D, Jacobs MA, El-Khouli R, Stojanovic D, Macura KJ. Advancements in MR imaging of the prostate: from diagnosis to interventions. *Radiographics* 2011;31:677–703.
- [12] Ng CS, Waterton JC, Kundra V, Brammer D, Ravoori M, Han L, et al. Reproducibility and comparison of DCE-MRI and DCE-CT perfusion parameters in a rat tumor model. *Technol Cancer Res Treat* 2012;11:279–88.
- [13] Li X, Huang W, Rooney WD. Signal-to-noise ratio, contrast-to-noise ratio and pharmacokinetic modeling considerations in dynamic contrast-enhanced magnetic resonance imaging. *Magn Reson Imaging* 2012;30:1313–22.
- [14] Heye T, Davenport MS, Horvath JJ, Feuerlein S, Breault SR, Bashir MR, et al. Reproducibility of dynamic contrast-enhanced MR imaging. Part I. Perfusion characteristics in the female pelvis by using multiple computer-aided diagnosis perfusion analysis solutions. *Radiology* 2013;266:801–11.
- [15] Heye T, Merkle EM, Reiner CS, Davenport MS, Horvath JJ, Feuerlein S, et al. Reproducibility of dynamic contrast-enhanced MR imaging. Part II. Comparison of intra- and interobserver variability with manual region of interest placement versus semiautomatic lesion segmentation and histogram analysis. *Radiology* 2013;266:812–21.
- [16] Zhang N, Zhang L, Qiu B, Meng L, Wang X, Hou BL. Correlation of volume transfer coefficient Ktrans with histopathologic grades of gliomas. *J Magn Reson Imaging* 2012;36:355–63.
- [17] Heye T, Boll DT, Reiner CS, Bashir MR, Dale BM, Merkle EM. Impact of precontrast T10 relaxation times on dynamic contrast-enhanced MRI pharmacokinetic parameters: T10 mapping versus a fixed T10 reference value. *J Magn Reson Imaging* 2014;39:1136–45.
- [18] Huang W, Chen Y, Fedorov A, Li X, Jajamovich GH, Malyarenko DI, et al. The impact of arterial input function determination variations on prostate dynamic contrast-enhanced magnetic resonance imaging pharmacokinetic modeling: a multicenter data analysis challenge. *Tomography* 2016;2:56–66.
- [19] Sanz-Requena R, Martí-Bonmati L, Pérez-Martínez R, García-Martí G. Dynamic contrast-enhanced case-control analysis in 3T MRI of prostate cancer can help to characterize tumor aggressiveness. *Eur J Radiol* 2016;85:2119–26.
- [20] Dikaïos N, Atkinson D, Tudisca C, Purpura P, Forster M, Ahmed H, et al. A comparison of Bayesian and non-linear regression methods for robust estimation of pharmacokinetics in DCE-MRI and how it affects cancer diagnosis. *Comput Med Imaging Graph* 2017;56:1–10.
- [21] Keil VC, Mädlar B, Gieseke J, Fimmers R, Hattingen E, Schild HH, et al. Effects of arterial input function selection on kinetic parameters in brain dynamic contrast-enhanced MRI. *Magn Reson Imaging* 2017;40:83–90.
- [22] Simoncic U, Leibfarth S, Welz S, Schwenzer N, Schmidt H, Reischl G, et al. Comparison of DCE-MRI kinetic parameters and FMISO-PET uptake parameters in head and neck cancer patients. *Med Phys* 2017;44:2358–68.
- [23] Chen X, Xie T, Fang J, Xue W, Tong H, Kang H, et al. Quantitative in vivo imaging of tissue factor expression in glioma using dynamic contrast-enhanced MRI derived parameters. *Eur J Radiol* 2017;93:236–42.
- [24] Ocaik I, Bernardo M, Metzger G, Barrett T, Pinto P, Albert PS, et al. Dynamic contrast-enhanced MRI of prostate cancer at 3 T: a study of pharmacokinetic parameters. *AJR Am J Roentgenol* 2007;189:849.
- [25] Alonzi R, Padhani AR, Allen C. Dynamic contrast enhanced MRI in prostate cancer. *Eur J Radiol* 2007;63:335–50.
- [26] Oto A, Yang C, Kayhan A, Tretiakova M, Antic T, Schmid-Tannwald C, et al. Diffusion-weighted and dynamic contrast-enhanced MRI of prostate cancer: correlation of quantitative MR parameters with Gleason score and tumor angiogenesis. *AJR Am J Roentgenol* 2011;197:1382–90.
- [27] Fedorov A, Fluckiger J, Ayers GD, Li X, Gupta SN, Tempany C, et al. A comparison of two methods for estimating DCE-MRI parameters via individual and cohort based AIFs in prostate cancer: a step towards practical implementation. *Magn Reson Imaging* 2014;32:321–9.
- [28] Fennessy FM, Fedorov A, Penzkofer T, Kim KW, Hirsch MS, Vangel MG, et al. Quantitative pharmacokinetic analysis of prostate cancer DCE-MRI at 3T: comparison of two arterial input functions on cancer detection with digitized whole mount histopathological validation. *Magn Reson Imaging* 2015;33:886–94.
- [29] Papoulis A. Probability, Random Variables, and Stochastic Processes. McGraw-Hill; 1965.
- [30] Levenberg KA. Method for the solution of certain non-linear problems in least squares. *Q Appl Math* 1944;11:164–8.
- [31] Marquardt DW. An algorithm for least-squares estimation of nonlinear parameters. *J Soc Ind Appl Math* 1963;11:431–41.
- [32] Murase K. Efficient method for calculating kinetic parameters using T1-weighted dynamic contrast-enhanced magnetic resonance imaging. *Magn Reson Med* 2004;51:858–62.
- [33] Ahearn TS, Staff RT, Redpath TW, Semple SIK. The use of the Levenberg-Marquardt curve-fitting algorithm in pharmacokinetic modelling of DCE-MRI data. *Phys Med Biol* 2005;50:N85–92.
- [34] Kallehaugue JF, Sourbron S, Irving B, Tanderup K, Schnabel JA, Chappell MA. Comparison of linear and nonlinear implementation of the compartmental tissue uptake model for dynamic contrast-enhanced MRI. *Magn Reson Med* 2017;77:2414–23.
- [35] Flouri D, Lesnic D, Sourbron SP. Fitting the two-compartment model in DCE-MRI by linear inversion. *Magn Reson Med* 2016;76:998–1006.
- [36] Feng D, Ho D, Chen K, LC Wu, Wang JK, Liu RS, et al. An evaluation of the algorithms for determining local cerebral metabolic rates of glucose using positron emission tomography dynamic data. *IEEE Trans Med Imaging* 1995;14:697–710.
- [37] Golub GH, Pereyra V. The differentiation of pseudo-inverses and nonlinear least squares problems whose variables separate. *SIAM J Numer Anal* 1973;10:413–32.
- [38] Boada F, Liang Z-P, Haacke EM. Improved parametric reconstruction using variable projection optimization. *Inverse Prob* 1998;14:19–27.
- [39] van der Veen JWC, de Beer R, Luyten PR, van Ormondt D. Accurate quantification of  $^{31}\text{P}$  NMR signals using the variable projection method and prior knowledge. *Magn Reson Med* 1988;6:92–8.
- [40] Sima DM, Van Huffel S. Separable nonlinear least squares fitting with linear bound constraints and its application in magnetic resonance spectroscopy data quantification. *J Comput Appl Math* 2007;203:264–78.
- [41] Mullen KM, van Stokkum IHM. The variable projection algorithm in time-resolved spectroscopy, microscopy and mass spectrometry applications. *Numer Algorithms* 2009;51:319–40.
- [42] Haldar JP, Anderson J, Sun S. Maximum likelihood estimation of T1 relaxation parameters using VARPRO. *Proc 15th Annu Meet ISMRM*. 2007. p. 41.
- [43] Trzasko JD, Mostardi PM, Riederer SJ, Manduca A. Estimating T1 from multi-channel variable flip angle SPGR sequences. *Magn Reson Med* 2013;69:1787–94.
- [44] Rauscher I, Eiber M, Ganter C, Martirosian P, Safi W, Umgelter A, et al. Evaluation of T1p as a potential MR biomarker for liver cirrhosis: comparison of healthy control subjects and patients with liver cirrhosis. *Eur J Radiol* 2014;83:900–4.
- [45] Hernando D, Haldar JP, Sutton BP, Ma J, Kellman P, Liang Z-P. Joint estimation of water/fat images and field inhomogeneity map. *Magn Reson Med* 2008;59:571–80.
- [46] Hernando D, Kellman P, Haldar JP, Liang Z-P. Robust water/fat separation in the presence of large field inhomogeneities using a graph cut algorithm. *Magn Reson Med* 2010;63:79–90.
- [47] Bydder M, Yokoo T, Yu H, Carl M, Reeder SB, Sirlin CB. Constraining the initial phase in water-fat separation. *Magn Reson Imaging* 2011;29:216–21.
- [48] Yin X, Guo Y, Li W, Huo E, Zhang Z, Nicolai J, et al. Chemical shift MR imaging methods for the quantification of transcatheter lipiodol delivery to the liver: pre-clinical feasibility studies in a rodent model. *Radiology* 2012;263:714–22.
- [49] Berglund J, Kullberg J. Three-dimensional water/fat separation and T2\* estimation based on whole-image optimization—application in breathhold liver imaging at 1.5 T. *Magn Reson Med* 2012;67:1684–93.
- [50] Stinson EG, Trzasko JD, Fletcher JG, Riederer SJ. Dual echo Dixon imaging with a constrained phase signal model and graph cuts reconstruction. *Magn Reson Med* 2017;78:2203–15.
- [51] Zhao B, Setsompop K, Ye H, Cauley SF, Wald LL. Maximum likelihood reconstruction for magnetic resonance fingerprinting. *IEEE Trans Med Imaging* 2016;35:1812–23.
- [52] Riabkov DY, Di Bella EVR. Estimation of kinetic parameters without input functions: analysis of three methods for multichannel blind identification. *IEEE Trans Biomed Eng* 2002;49:1318–27.
- [53] Riabkov DY, Di Bella EVR. Blind identification of the kinetic parameters in three-compartment models. *Phys Med Biol* 2004;49:639–64.
- [54] National Cancer Institute. Prostate Cancer—Patient Version. <https://www.cancer.gov/types/prostate>.
- [55] Delongchamps NB, Rouanne M, Flam T, Beuvon F, Liberatore M, Zerbib M, et al. Multiparametric magnetic resonance imaging for the detection and localization of prostate cancer: combination of T2-weighted, dynamic contrast-enhanced and diffusion-weighted imaging. *BJU Int* 2011;107:1411–8.
- [56] De Rooij M, Hamoen EHH, Fütterer JJ, Barentsz JO, Rovers MM. Accuracy of multiparametric MRI for prostate cancer detection: a meta-analysis. *Am J Roentgenol* 2014;202:343–51.
- [57] Weinreb JC, Barentsz JO, Choyke PL, Cornud F, Haider MA, Macura KJ, et al. PI-RADS prostate imaging – reporting and data system: 2015, version 2. *Eur Urol*

- 2016;69:16–40.
- [58] Kershaw LE, Buckley DL. Precision in measurements of perfusion and microvascular permeability with T1-weighted dynamic contrast-enhanced MRI. *Magn Reson Med* 2006;56:986–92.
- [59] Fennessy FM, Fedorov A, Gupta SN, Schmidt EJ, Tempny CM, Mulkern RV. Practical considerations in T1 mapping of prostate for dynamic contrast enhancement pharmacokinetic analyses. *Magn Reson Imaging* 2012;30:1224–33.
- [60] Winfield JM, Payne GS, Weller A, DeSouza NM. DCE-MRI, DW-MRI, and MRS in cancer: challenges and advantages of implementing qualitative and quantitative multi-parametric imaging in the clinic. *Top Magn Reson Imaging* 2016;25:245–54.
- [61] Bansal S, Gupta NP, Yadav R, Khera R, Ahlawat K, Gautam D, et al. Multiparametric magnetic resonance imaging-transrectal ultrasound fusion prostate biopsy: a prospective, single centre study. *Indian J Urol* 2017;33:134–9.
- [62] Rouvière O, Vitry T, Lyonnet D. Imaging of prostate cancer local recurrences: why and how? *Eur Radiol* 2010;20:1254–66.
- [63] Kitajima K, Murphy RC, Nathan MA, Froemming AT, Hagen CE, Takahashi N, et al. Detection of recurrent prostate cancer after radical prostatectomy: comparison of 11C-Choline PET/CT with pelvic multiparametric MR imaging with endorectal coil. *J Nucl Med* 2014;55:223–32.
- [64] Kargar S, Stinson EG, Borisch EA, Froemming AT, Kawashima A, Mynderse LA. Robust and efficient pharmacokinetic parameter estimation: Application to prostate DCE-MRI, ISMRM. *Proc Intl Soc Mag Reson Med* 2016:2463.
- [65] Kargar S, Stinson EG, Borisch EA, Froemming AT, Kawashima A, Mynderse LA, et al. Robust and efficient perfusion parameter estimation for DCE-MRI of the prostate utilizing the variable projection (VARPRO) method. *Proc Intl Soc Mag Reson Med* 2017:4385.
- [66] Coveney PV. Scientific grid computing. *Philos Trans A Math Phys Eng Sci* 2005;363:1707–13.
- [67] Froemming AT, Borisch EA, Trzasko JD, Grimm RC, Manduca A, Young P, et al. The application of sparse reconstruction to high spatio-temporal resolution dynamic contrast enhanced MRI of the prostate: initial clinical experience with effect on image and parametric perfusion characteristic quality. *Proc Intl Soc Mag Reson Med* 2015:1169.
- [68] Haider CR, HH Hu, Campeau NG, Huston J, Riederer SJ. 3D high temporal and spatial resolution contrast-enhanced MR angiography of the whole brain. *Magn Reson Med* 2008;60:749–60.
- [69] Riederer SJ, Tasciyan T, Farzaneh F, Lee JN, Wright RC, Herfkens RJ. MR fluoroscopy: technical feasibility. *Magn Reson Med* 1988;8:1–15.
- [70] Frahm J, Haase A, Matthaei D. Rapid NMR imaging of dynamic processes using the FLASH technique. *Magn Reson Med* 1986;3:321–7.
- [71] de Bazelaire CM, Duhamel GD, Rofsky NM, Alsop DC. MR imaging relaxation times of abdominal and pelvic tissues measured in vivo at 3.0 T: preliminary results. *Radiology* 2004;230:652–9.
- [72] Parker GJM, Roberts C, Macdonald A, Buonaccorsi GA, Cheung S, Buckley DL, et al. Experimentally-derived functional form for a population-averaged high-temporal-resolution arterial input function for dynamic contrast-enhanced MRI. *Magn Reson Med* 2006;56:993–1000.
- [73] NEMA standards publication MS 1-2008 (R2014) determination of signal-to-noise ratio (SNR) in diagnostic magnetic resonance imaging. 2008. 2008. p. 1–19.
- [74] Thornbury JR, Eugene W. Caldwell lecture. Clinical efficacy of diagnostic imaging: love it or leave it. *AJR Am J Roentgenol* 1994;162:1–8.
- [75] Gill AB, Black RT, Bowden DJ, Priest AN, Graves MJ, Lomas DJ. An investigation into the effects of temporal resolution on hepatic dynamic contrast-enhanced MRI in volunteers and in patients with hepatocellular carcinoma. *Phys Med Biol* 2014;59:3187–200.